Electronic Supplementary Material (ESI) for Materials Horizons.
This journal is © The Royal Society of Chemistry 2020

Electronic Supplementary Material (ESI) for Materials Horizons.
This journal is © The Royal Society of Chemistry 2019

Organic Intercalation Engineering of Quasi-2D Dion-Jacobson α-$CsPbI_3$ Perovskites

Zhi Fang, Minghui Shang, Yapeng Zheng, Tian Zhang, Zhentao Du, Gang Wang, Xiangmei Duan, Kuo-Chih Chou, Chun-Ho Lin, Weiyou Yang*, Xinmei Hou* and Tom Wu*

Computational Methods

Density Functional Theory Calculations

Crystal structures, electronic and optical properties were computed employing density functional theory (DFT) based on Perdew-Burke-Ernzerhof (PBE) functional,[1] as implemented in Vienna Ab-initio Simulation Package (VASP).[2] The electron-ion interaction was described by the projector-augemented wave (PAW) potentials with a kinetic energy cutoff 450 eV[3] confirmed by convergence test. The valence electron configurations for Cs, Pb, I, C, N and H were $5s^2 5p^6 6s^1$, $6s^2 6p^2$, $5s^2 5p^5$, $2s^2 2p^2$, $2s^2 2p^3$ and $1s^1$, respectively. The non-local van der Waals (vdW) interactions was corrected with zero damping DFT-D3 method of Grimme[4, 5] and the dipole corrections along z axis of slabs were considered.[6] The convergence threshold for self-consistent-field (SCF) iteration was set at 1.0×10^{-5} eV, and the atoms were allowed to relax until all the force components decrease to below 0.05 eV/Å. The integration within running over the Brillion zoon of $(EDA)Cs_{n-1}Pb_nI_{3n+1}$ (n = 1, 2, 3, 4, 5, 6, 8 and 50) PVSKs with various inorganic layer numbers of n was sampled by 3×3×4, 3×3×2, 3×3×2, 3×3×2, 3×3×1, 3×3×1, 3×3×1 and 3×3×1 k-point meshes centered at the Γ point, respectively. The line-mode k-point path was utilized for the band structure simulation with 32 k-points between high symmetric points. The inorganic layer number of the model for the PVSK (n = 50) is 6, with the middle 2 inorganic layers fixed to simulate multilayer α-$CsPbI_3$ bulk with inorganic layers of ~50. Its bandgap is calculated to be 1.497 eV and the simulated layer number ($n \approx 50$) is obtained by substituting the E_g value into the linear fitting equation above.

Ab Initio Molecular Dynamics Simulation

Ab initio molecular dynamics (AIMD) simulation were carried out employing a canonical (NVT) ensemble with a Nosé-Hoover thermostat[7] under 300 K, as implemented in the VASP, with a timestep of 1 fs and a running time of 5 ps. PAW potentials were also used, with a plane-wave cutoff energy of 450 eV, an energy threshold of 10^{-5} eV, and a single k point at the Γ.

Formation Enthalpy (ΔH_{form})

The lattice distortion is directly correlated with the transformation of perovskite phase and the structural stability. The stability of $(EDA)Cs_{n-1}Pb_nI_{3n+1}$ PVSKs can be evaluated based on formation enthalpy (ΔH_{form}),[8-10] which is set by:

$$\Delta H_{form} = \frac{E_{(\mathrm{EDA})Cs_{n-1}Pb_nI_{3n+1}} - (n-1)E_{CsPbI_3} - E_{EDAPbI_4}}{n} \tag{1}$$

where $E_{(\mathrm{EDA})Cs_{n-1}Pb_nI_{3n+1}}$, E_{CsPbI_3} and E_{EDAPbI_4} refer to the DFT total energies of $(EDA)Cs_{n-1}Pb_nI_{3n+1}$, α-$CsPbI_3$ and $EDAPbI_4$ PVSKs per unit cell, respectively. ΔH_{form} represents the stability of $(EDA)Cs_{n-1}Pb_nI_{3n+1}$ PVSK alloys referencing $CsPbI_3$ and $EDAPbI_4$ components, whose boundary condition is $2 \leq n < \infty$ (n is an integer). If n is 1 or ∞, the ΔH_{form} of $CsPbI_3$ and $EDAPbI_4$ is equal to 0, indicating the same stability of $CsPbI_3$ and $EDAPbI_4$, which implies that n cannot be set as 1 or ∞. Therefore, in our work, the ΔH_{form} is used to evaluate the stability of the PVSKs with $2 \leq n < \infty$ except $EDAPbI_4$ (n=1) and $CsPbI_3$ (n=∞).

Decomposition Energy (ΔH_{decom})

It is known that, in air conditions, the (EDA)$Cs_{n-1}Pb_nI_{3n+1}$ PVSKs would be decomposed into $EDAI_2$ + CsI + PbI_2.[11] Thereby, the decomposition energy (ΔH_{decom}) can be set by:[11]

$$\Delta H_{decom} = \frac{nE_{PbI_2} + (n-1)E_{CsI} + E_{EDAI_2} - E_{(\mathrm{EDA})Cs_{n-1}Pb_nI_{3n+1}}}{n} \tag{2}$$

where E_{PbI_2} and E_{CsI} are the energies of bulk PbI_2 and CsI, and E_{EDAI_2} is the energy of gas phase of $EDAI_2$.

Carrier Effective Mass and Exciton Binding Energy

The electron effective mass (m_e^*) and hole effective mass (m_h^*) of (EDA)$Cs_{n-1}Pb_nI_{3n+1}$ PVSKs were calculated using parabolic band fitting approach around the *CBM* or *VBM*, according to following equations (see Figure S37):

$$\left(m^*\right)_{ij} = \hbar^2 \left[\frac{\partial^2 \varepsilon_n\left(\vec{k}\right)}{\partial k_i k_j}\right]^{-1}, i, j = x, y, z \tag{3}$$

where m^* is the effective mass of the charge carrier, i and j denote reciprocal components, $\varepsilon_n\left(\vec{k}\right)$ is the energy dispersion function of the n^{th} band, $\vec{k}$ is the wave vector, and $\hbar$ represents the reduced Planck constant. For better fitting parabolic within the *VBM* and *CBM* regions, the nonself-consistent calculation for band structure was performed using 41 *k*-points around *VBM* or *CBM* with a separation of 0.005 Å^{-1}.

The exciton binding energy (E_b) can be calculated by the following Wannier exciton model:[12-15]

$$E_b = \frac{\mu^* R_y}{m_0 \varepsilon_r^2} \tag{4}$$

where μ^* is the reduced exciton mass (*i.e.* $1/\mu^* = 1/m_e + 1/m_h$), R_y is the atomic Rydberg energy, and ε_r is the relative dielectric constant (the high-frequency limit of dielectric constant (ε_∞) caused by electronic polarization).

Evaluation of PCE

For EDA-based PVSKs (n = 1-6, 8, 50) and α-$CsPbI_3$ PVSK solar cells, the open-circuit voltage (V_{OC}), short-circuit current (J_{SC}) and PCE are calculated based on their bandgaps (E_g). The J_{SC} can be estimated by assuming that all photons with energy larger than E_g are absorbed by the PVSKs for the generation of electron-hole pairs, using the equation:[16-18]

$$J_{SC} = e\int_{E_g}^{\infty} \frac{S(E)}{E} dE \tag{5}$$

where e and E and are the electronic charge and the energy of an incident photon, respectively. $S(E)$ represents the power radiated by the sun on the earth per unit area and per unit photon energy (unit: W·m^{-3}·eV^{-1}), as shown in Figure S44.

The V_{OC} can be calculated according to the bandgap of PVSKs and the loss-in-potential E_{loss} as:

$$V_{OC} = \left(E_g - E_{loss}\right) / e \tag{6}$$

where E_{loss} is set to 0.5 eV.[16, 17]

Finally, based on the calculation of V_{OC} and J_{SC}, the PCE as a function of the bandgap can be estimated by:

$$\eta\left(E_g\right) = \frac{FF \times J_{SC} \times V_{OC}}{P_{sun}} \tag{7}$$

where FF is the fill factor and set to be of 74%.[19] P_{sun} is the total incident power, which is calculated by $p_{sun} = \int_0^{\infty} S\left(E\right) dE$.[20]

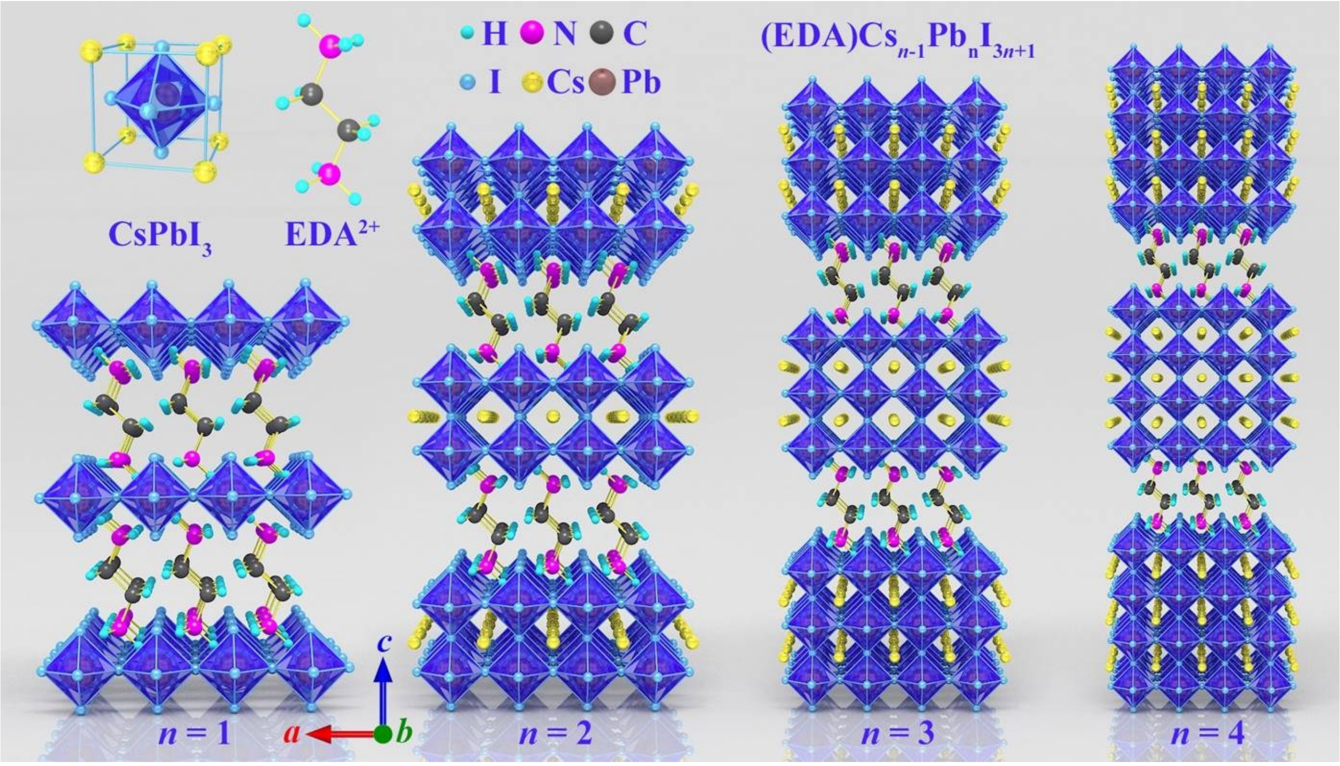

Figure S1. The structure models of quasi-2D DJ (EDA)$Cs_{n-1}Pb_nI_{3n+1}$ PVSKs from n = 1 to 4. The structures of $CsPbI_3$ unit and cation EDA^{2+} are given in the upper-left corner.

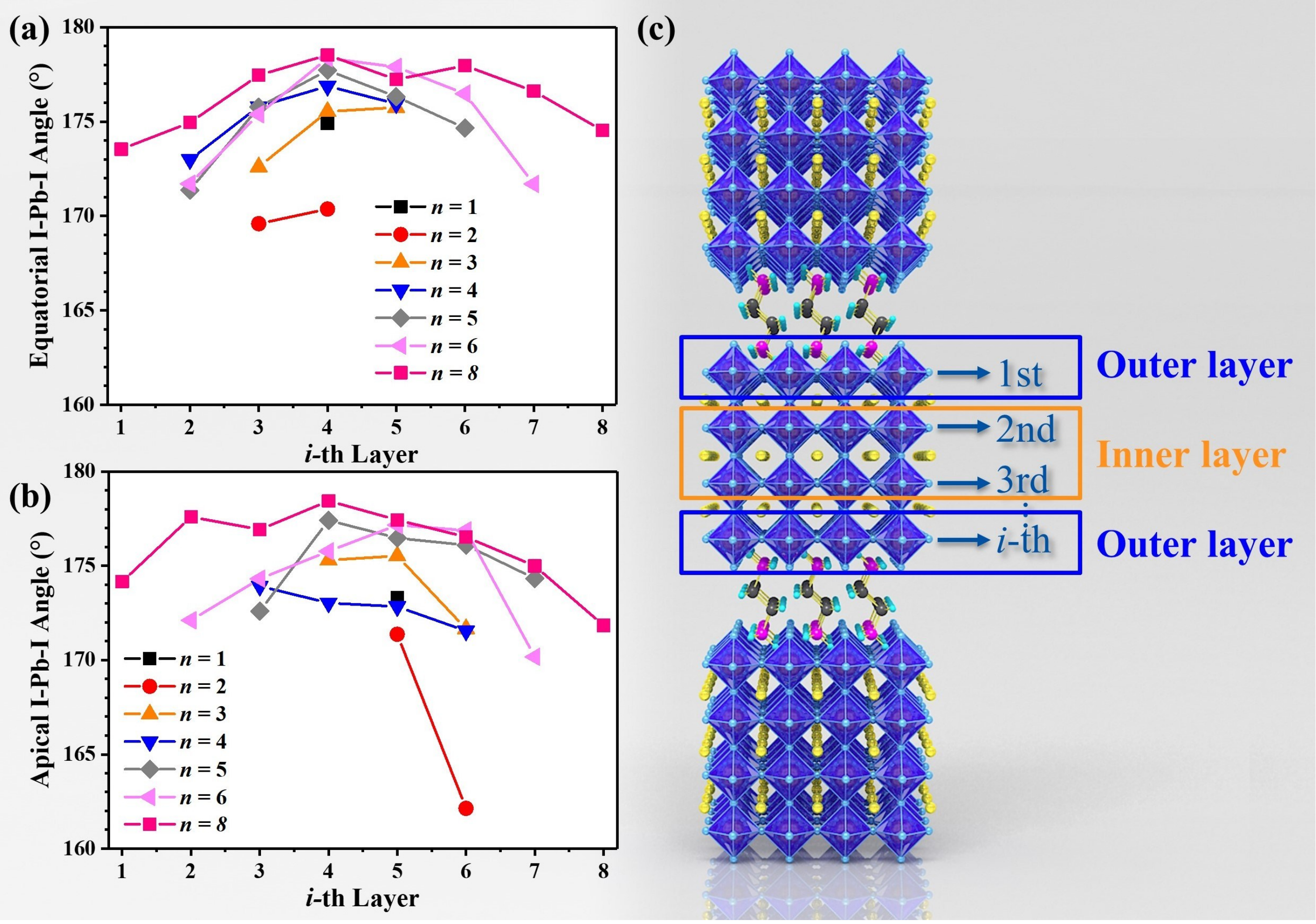

Figure S2. (a-b) Equatorial and apical I-Pb-I angles of each inorganic layer for (EDA)$Cs_{n-1}Pb_nI_{3n+1}$ PVSKs with different *n* values. (c) Illustration on serial numbers of i^{th} inorganic layer and the definition of outer and inner layer.

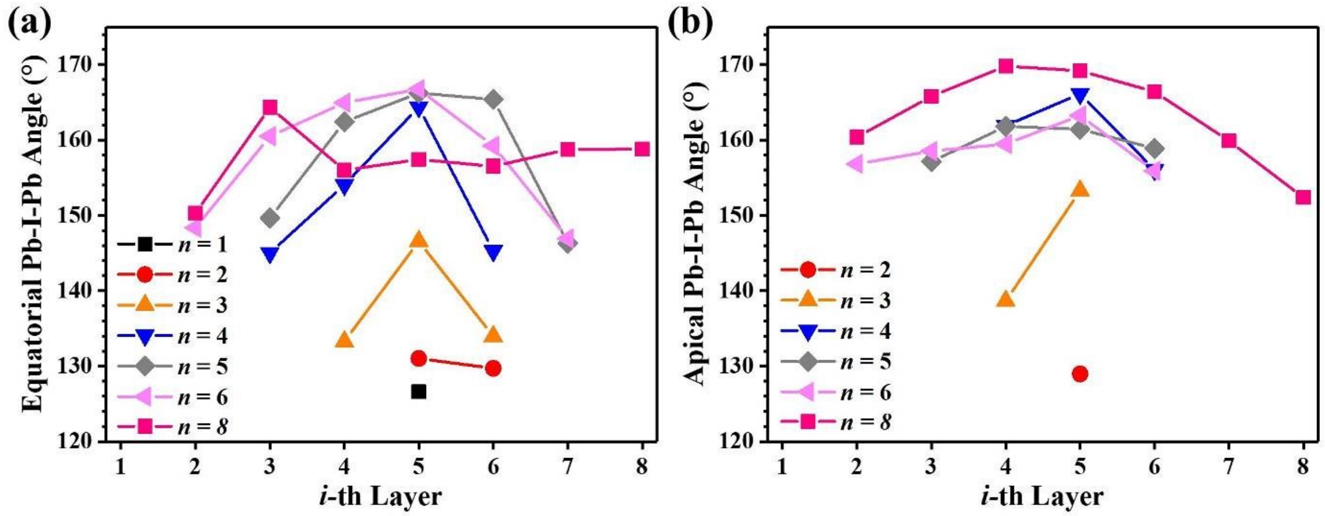

Figure S3. (a-b) Equatorial and apical Pb-I-Pb angles of each inorganic layer for (EDA)$Cs_{n-1}Pb_nI_{3n+1}$ PVSKs with different *n* values.

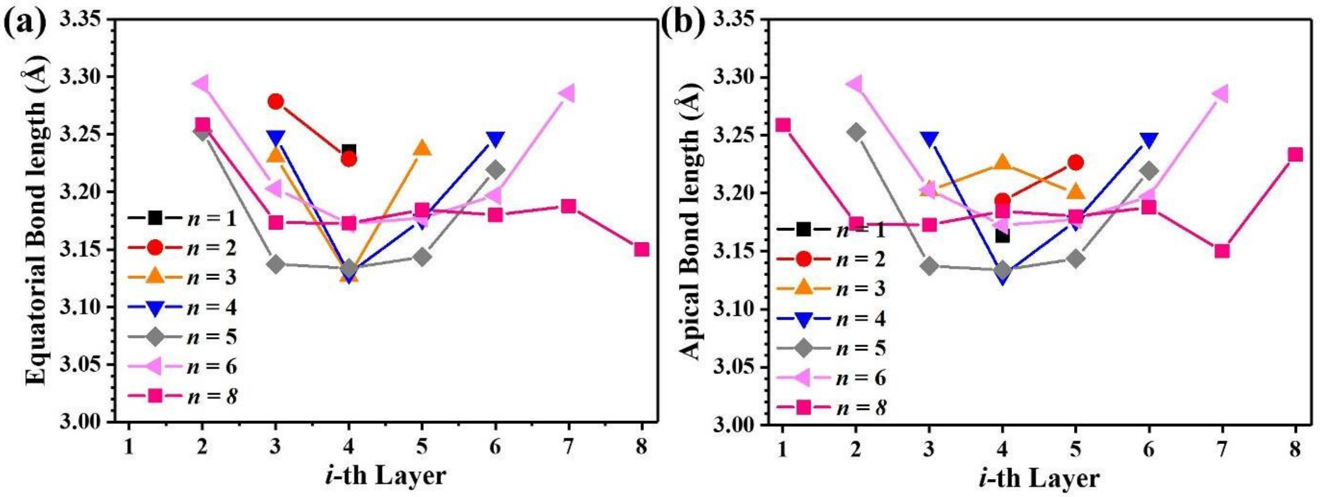

Figure S4. (a-b) Equatorial and apical Pb-I bonds of each inorganic layer for (EDA)$Cs_{n-1}Pb_nI_{3n+1}$ PVSKs with different *n* values.

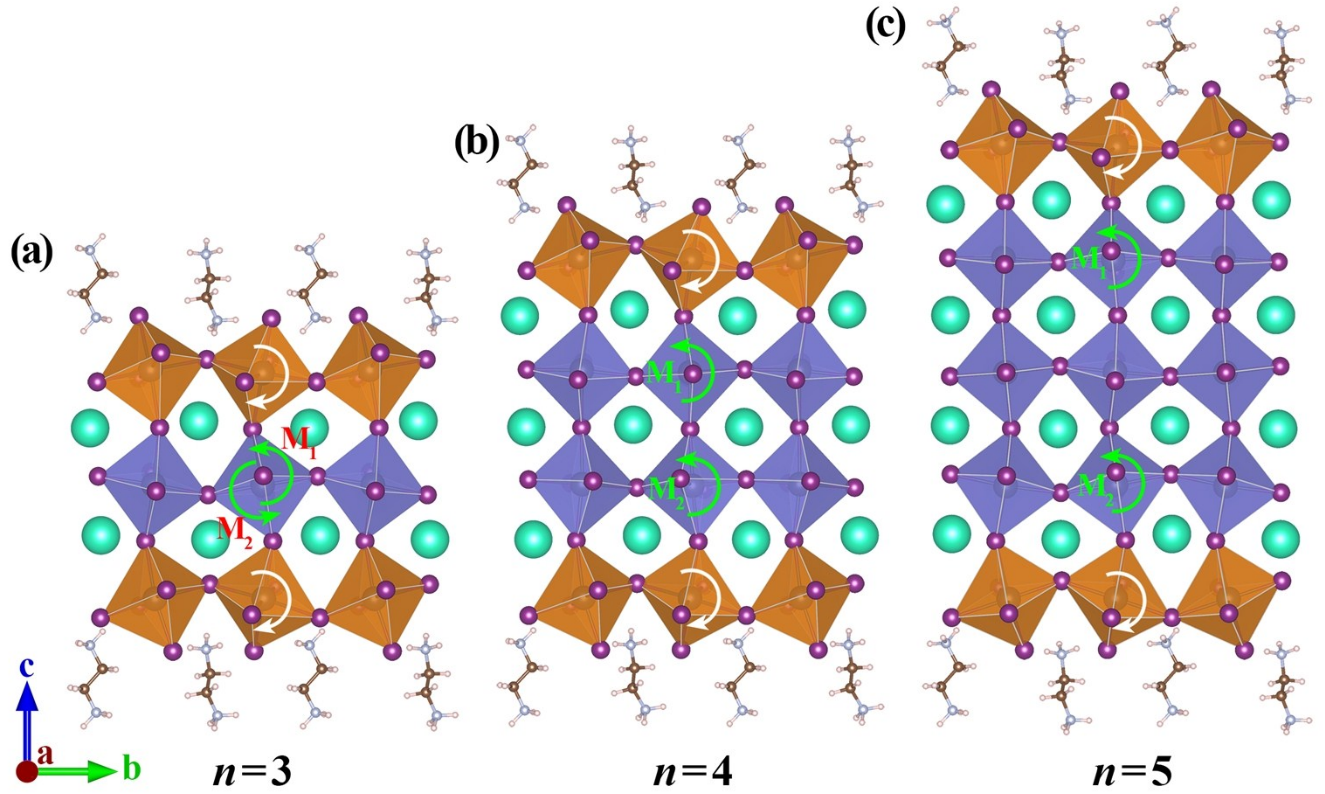

Figure S5. (a-c) The optimized structures for the quasi-2D PVSKs with *n* = 3, 4 and 5, respectively. The orange and purple octahedra refer outer and inner layers, respectively.

As shown in Figure 1h, *n* = 4 is regarded as the turning point with significantly reduced lattice distortion for quasi-2D $CsPbI_3$ PVSKs. To clarify the intrinsic difference between *n* = 4 and *n* = 3, 5, we analyze the force moment of octahedral layers (see Figure S5). All the first outer layers (orange octahedron) directly interacting with organic cations have a huge rotation in the direction shown by the white arrows, which gives rise to force moments (labeled by green arrows) onto inner layers (purple octahedron). The difference among these PVSKs comes from the different buffer effect of the inner layers. For the PVSK with *n* = 3 (Figure S5a), taking an octahedron in the inner layer as an example, the two overlaid force moments with the same direction will enhance the distortion and drive it to rotate counterclockwise, leading to the heavy distortion of the inner layer. For the PVSK with *n* = 4 (Figure S5b), taking the middle two octahedra as an example, each receives only one external force moment. Besides, both are forced to rotate counterclockwise, which is mutually exclusive and brings much lighter distortion than that of the PVSK with *n* = 3. Herein, the buffer effect of the inner layer on the force moment for *n* = 4 is much strong than that of *n* = 3. With the increase of *n*, the thick inner layers also act as a buffer which can weaken the transmit of force and distortion. Thereby, the PVSKs with $n >$ 4 show less distortion than the models with $n \leq 3$. As mentioned above, *n* = 4 is the turning point of significantly reduced lattice distortion. What's more, Yu *et al.* reported the transformation from the confinement structures to structures without confinement in DJ-type PVSKs occurs at *n* = 4, which also proves the unique feature of the PVSK with *n* = 4.[21]

Accordingly, the PVSKs could be divided into two groups, *i.e.* the PVSKs ($n < 4$) with heavy lattice distortion and the PVSKs ($4 \leq n \leq 8$) with light lattice distortion. For the PVSKs with $n < 4$, the differentiation of lattice distortion is significant and the PVSKs with n =1-3 exhibit much more distortion than the PVSK with $n = 4$. As a result, the PVSK with $n = 4$ owns much better stability than that of n = 1-3, in agreement with the decomposition energy in Figure 2b. With respect to the PVSKs ($4 \leq n \leq 8$), though the $\angle$I-Pb-I of $n = 5$ is closer to 180° than that of $n = 4$, the apical $R_{\text{Pb-I}}$ of $n = 5$ is longer than that of $n = 4$. Compared to the PVSKs with $n < 4$, the PVSKs with $4 \leq n \leq 8$ exhibit similar lattice distortion (please see Figure 1g and h). In this circumstance, the intrinsic difference among these PVSKs is the change of inorganic layers. Smaller inorganic layers mean more organic cations, leading to stronger interaction between organic cations and inorganic layers, which contributes better phase stability. Accordingly, the stability follows the order: PVSK ($n = 4$) > ($n = 5$) > ($n = 6$) > ($n = 8$), as shown in Figure 2b. Thereby, the decomposition energy of $n = 4$ is higher than that of n = 5-8. Briefly, when the differentiation of lattice distortion is highly obvious ($n < 4$), less distortion with better stability the PVSKs has. When the lattice distortion is similar ($n \geq 4$), the smaller n endows a better stability. As the turning point of significantly reduced lattice distortion, the PVSK ($n = 4$) is considered as the most stable structure.

As shown in Figure 2b, the PVSK with $n = 2$ exhibits the lowest decomposition energy among n = 1-4. With respect to the larger lattice distortion, the PVSK with $n = 2$ exhibits poorer stability than that with $n = 3$ and 4, implying its lower decomposition energy. Though the $\angle$Pb-I-Pb of $n = 2$ is a little closer to 180° than that of $n = 1$, the $\angle$I-Pb-I and $R_{\text{Pb-I}}$ of $n = 2$ are much more different to that of α-$CsPbI_3$. That is to say, the lattice distortion of $n = 2$ is also larger than that of $n = 1$, representing its lower decomposition energy. Besides, the PVSK with $n = 2$ is the transition structure between 2D and quasi-2D PVSK. The abrupt transition from 2D to quasi-2D might leads to a metastable structure. It is also the smallest-n quasi-2D PVSK with a highest molar ratio of EDA:Cs, which might be most difficult to intercalate such a large number of EDA^{2+} cation into the $CsPbI_3$ crystal among EDA-based quasi-2D PVSKs. Briefly, the PVSK with $n = 2$ is the least stable structure with lowest decomposition energy among n = 1-4.

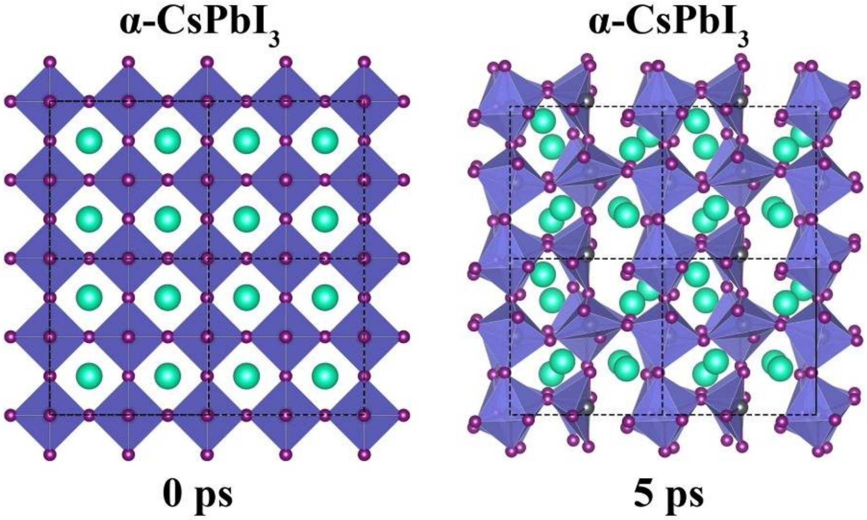

Figure S6. The structures of α-$CsPbI_3$ PVSK after *ab* initio molecular dynamics simulation (AIMD) at 0 and 5 ps under 300 K, respectively.

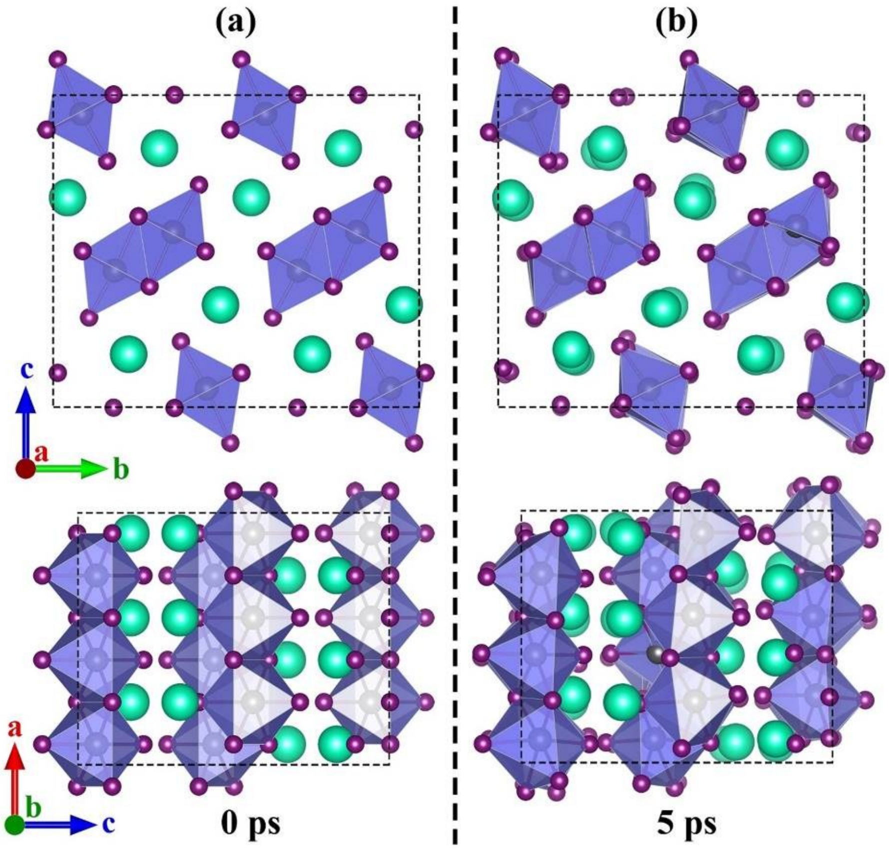

Figure S7. (a, b) The structures of δ-$CsPbI_3$ PVSK after AIMD simulation at 0 and 5 ps under 300 K, respectively.

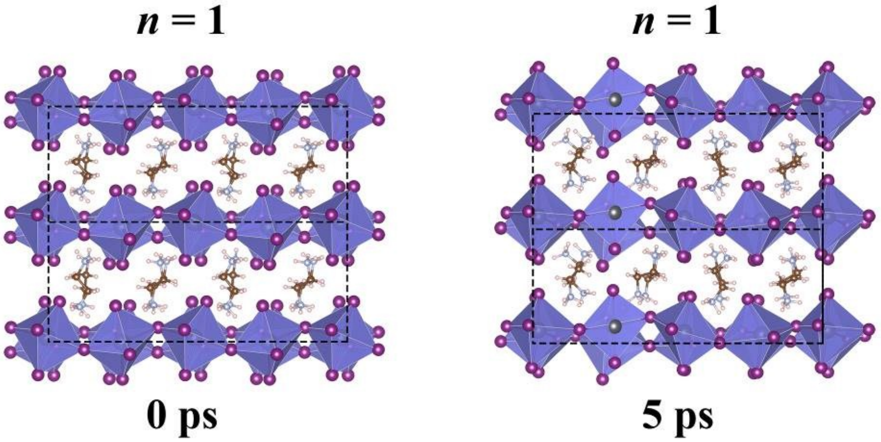

Figure S8. The structures of (EDA)$Cs_{n-1}Pb_nI_{3n+1}$ (n = 1) perovskites after AIMD simulation at 0 and 5 ps under 300 K, respectively.

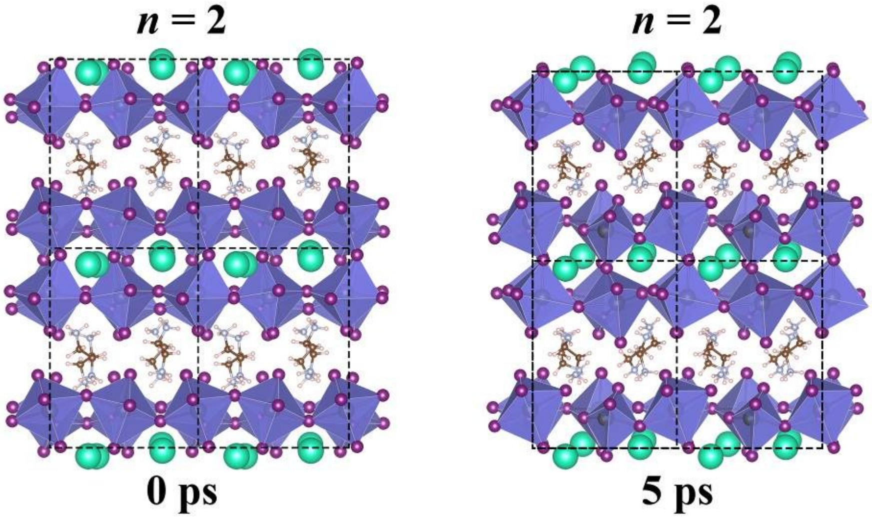

Figure S9. The structures of $(EDA)Cs_{n-1}Pb_nI_{3n+1}$ ($n = 2$) perovskites after AIMD simulation at 0 and 5 ps under 300 K, respectively.

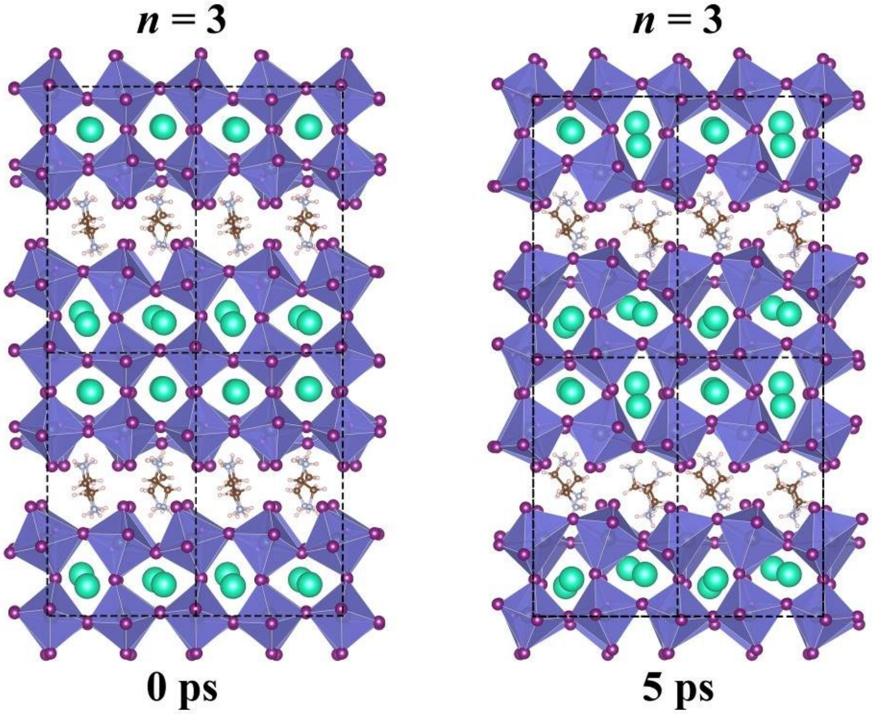

Figure S10. The structures of (EDA)$Cs_{n-1}Pb_nI_{3n+1}$ (n = 3) perovskites after AIMD simulation at 0 and 5 ps under 300 K, respectively.

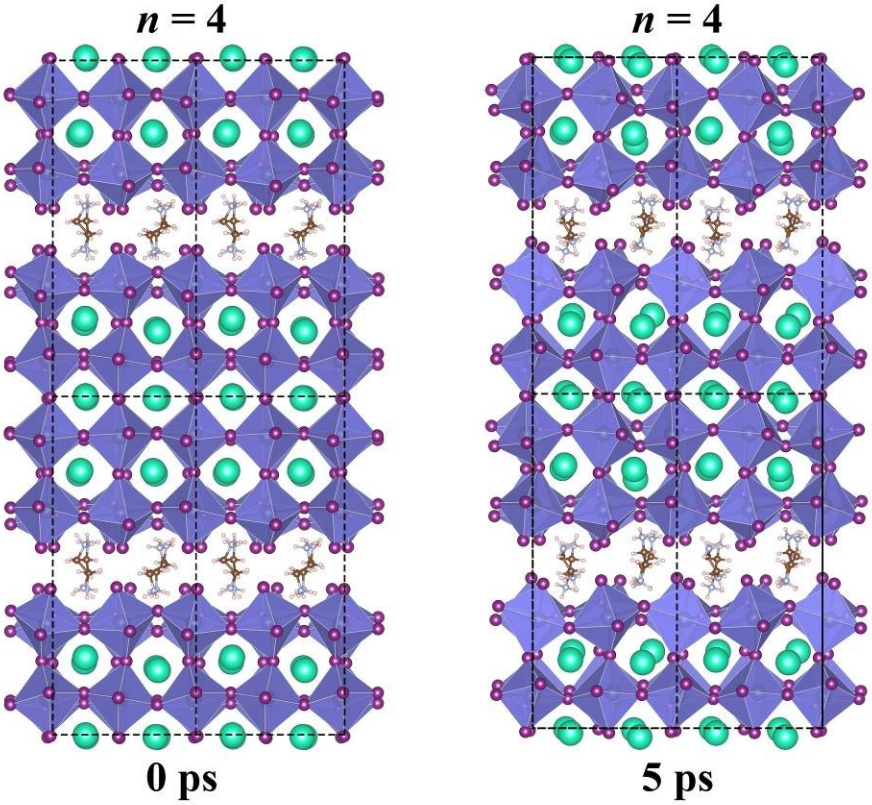

Figure S11. The structures of (EDA)$Cs_{n-1}Pb_nI_{3n+1}$ (n = 4) perovskites after AIMD simulation at 0 and 5 ps under 300 K, respectively.

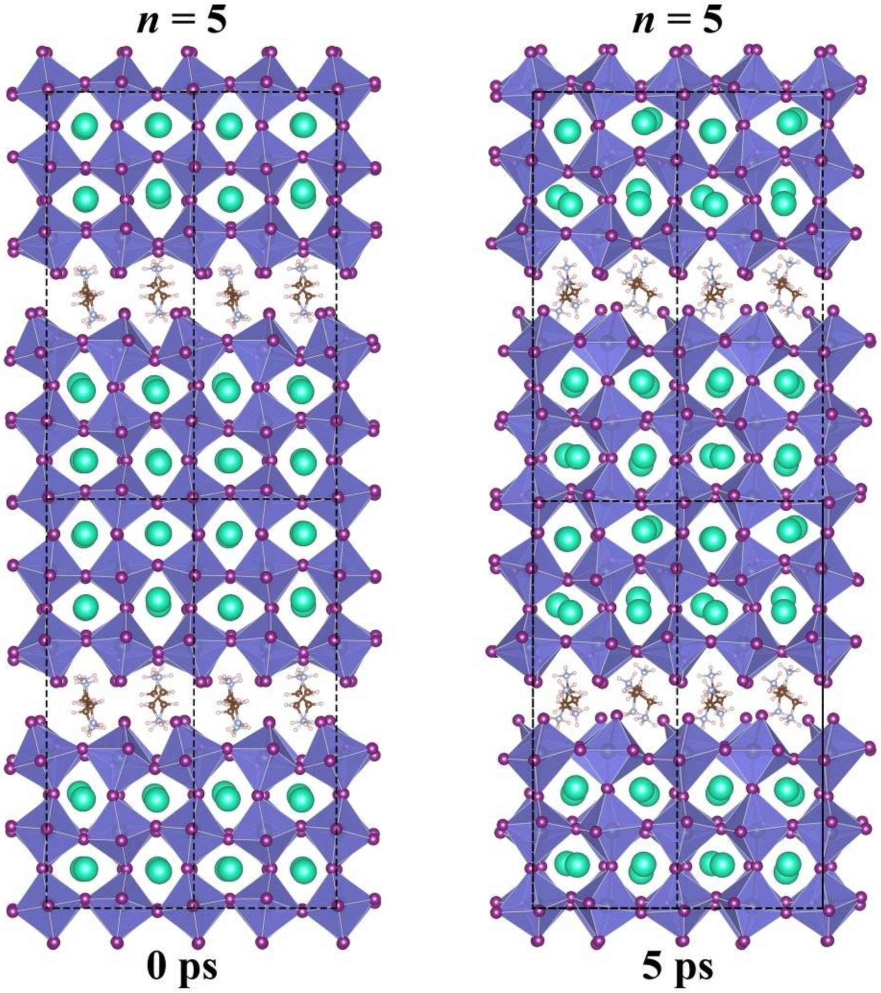

Figure S12. The structures of (EDA)$Cs_{n-1}Pb_nI_{3n+1}$ ($n = 5$) perovskites after AIMD simulation at 0 and 5 ps under 300 K, respectively.

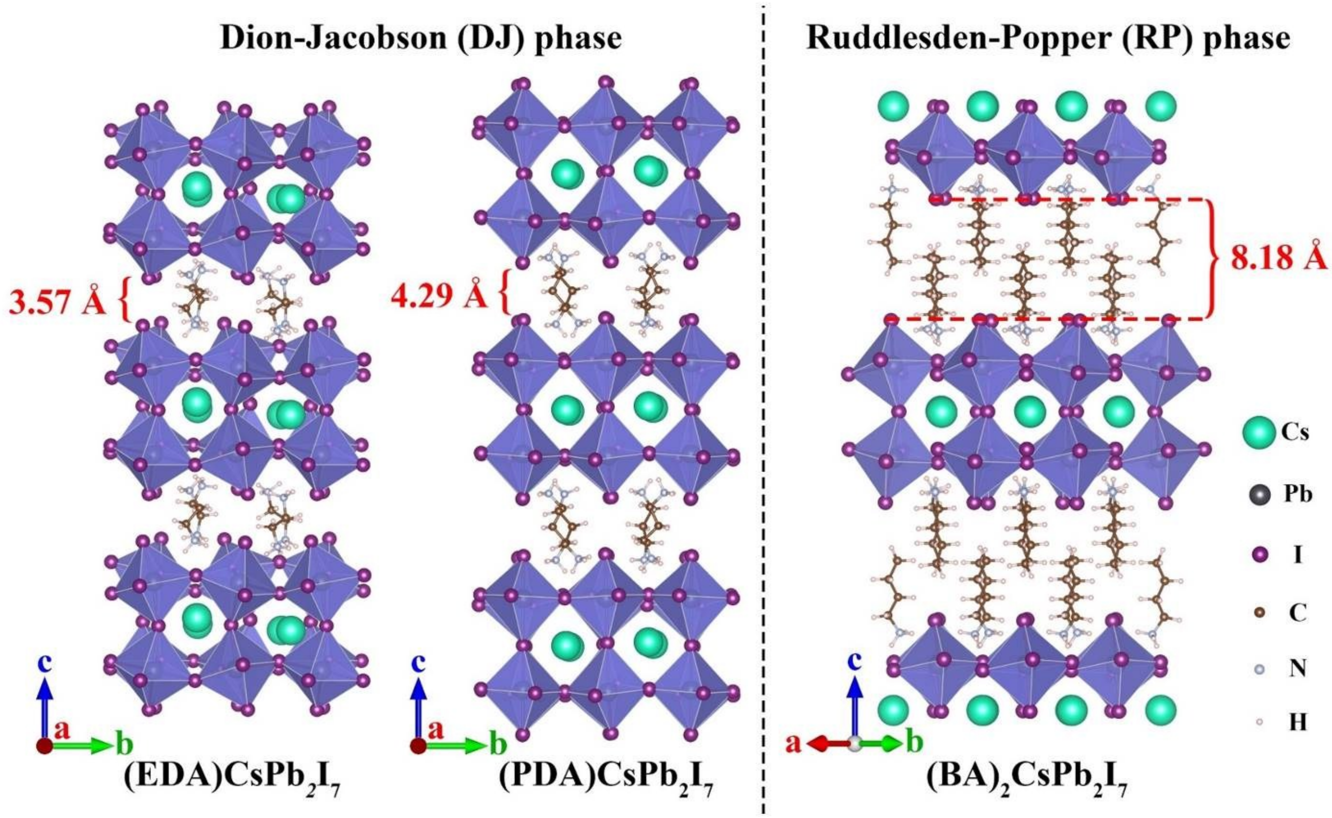

Figure S13. Interlayer distances between two neighboured inorganic layers for DJ phases of (EDA)$CsPb_2I_7$ and (PDA)$CsPb_2I_7$, as well as RP phase of $(BA)_2CsPb_2I_7$ PVSKs. EDA: ethylenediamine, PDA: propane-1,3-diammonium, BA: butyl ammonium. All these structures are optimized under identical parameters by first-principle calculation.

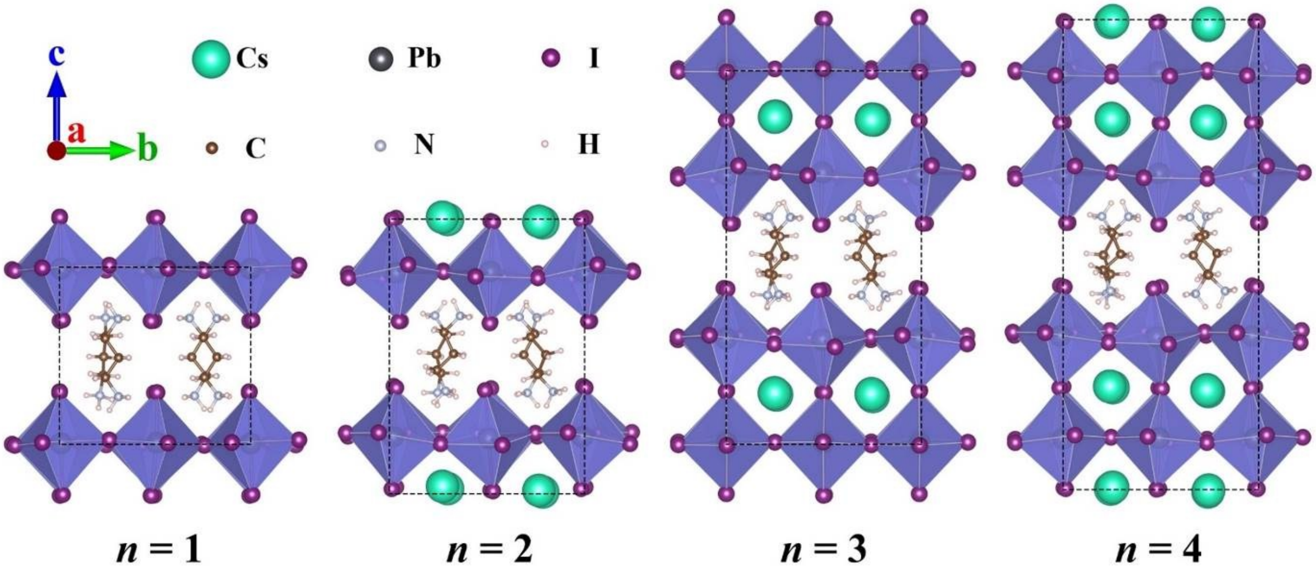

Figure S14. The optimized crystal structures of RP phase (PDA)$Cs_{n-1}Pb_nI_{3n+1}$ (n = 1, 2, 3, 4) PVSKs.

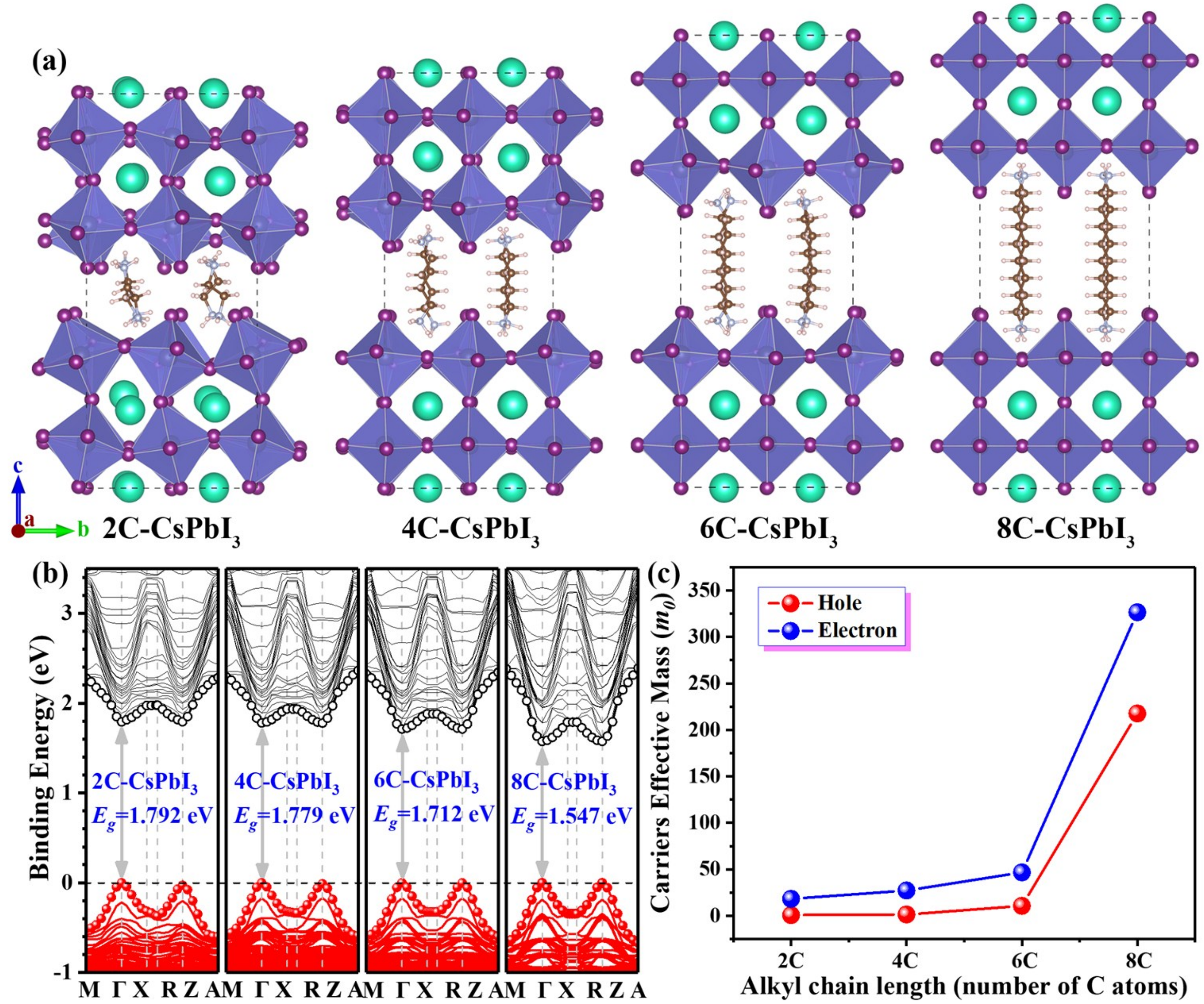

Figure S15. (a) The optimized unit cells of quasi-2D α-CsPbI$_3$ PVSKs (n = 4) intercalated by organic cations with different alkyl chain lengths, *e.g.* ethanediamine ($NH_2(CH_2)_2NH_2$), butanediamine ($NH_2(CH_2)_4NH_2$), hexamethylenediamine ($NH_2(CH_2)_6NH_2$) and diaminooctane ($NH_2(CH_2)_8NH_2$). (b) Calculated band structures. (c) Their corresponding out-of-plane (along c axis) carrier effective masses.

Fig. S15 shows the band structures and corresponding effective masses of quasi-2D α-CsPbI$_3$ PVSKs (n = 4) intercalated by organic cations with varying alkyl chain length, *e.g.* ethanediamine ($NH_2(CH_2)_2NH_2$), butanediamine ($NH_2(CH_2)_4NH_2$), hexamethylenediamine ($NH_2(CH_2)_6NH_2$) and diaminooctane ($NH_2(CH_2)_8NH_2$) (Fig. S15a). These PVSKs are referred by the number of carbon atom within the ligands, such as 2C-CsPbI$_3$, 4C-CsPbI$_3$, 6C-CsPbI$_3$ and 8C-CsPbI$_3$, respectively. Fig. S15b gives the band structures of these quasi-2D α-$CsPbI_3$ PVSKs, disclosing their direct bandgap. With increasing chain length, the bandgap gradually gets smaller, which can be attributed to the reduced lattice distortion. As shown in Figure R1a, the distance between two neighbored inorganic layers gets larger with the increase of organic chain length, then the interaction between two inorganic layers becomes weaker with reduced lattice distortion. Because the Pb 6s-I 5p antibonding coupling could be weakened by the heavier lattice distortion, the bandgap will get larger.[22] Accordingly, the bandgap can decrease by increasing the length of the organic cations. Even though the narrower bandgap favors the optical absorption, the increased interlayer distance and weak interaction between inorganic layers will severely hinder the charge transport, leading to a decreased performance of solar cell. As shown in Figure R1c, the out-of-plane (along *c* axis) carrier effective masses increase with the raise of alkyl chain length. The calculation result in Fig. S15c suggests that the limit of chain length before the performance dramatically decline is 6-C-atom diamine cations (*i.e.* $NH_2(CH_2)_6NH_2$).

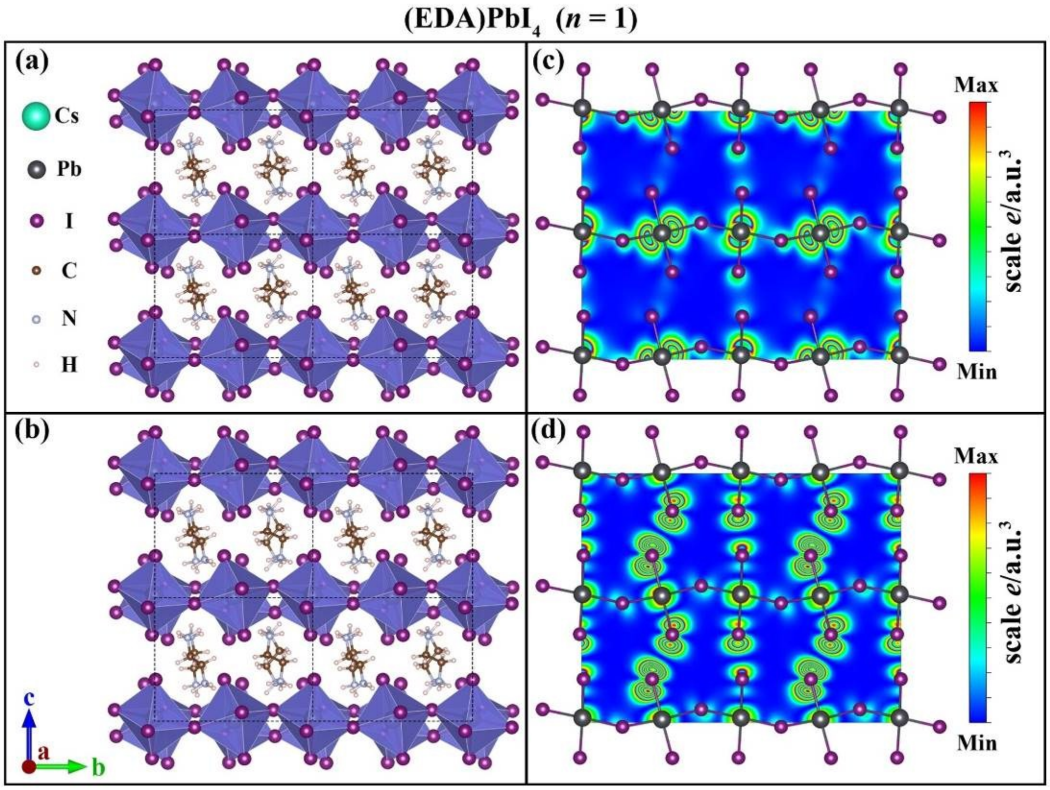

Figure S16. (a, b) The optimized polyhedron model of 1×2×2 supercell of (EDA)$Cs_{n-1}Pb_nI_{3n+1}$ (n = 1) from the view of *c* axis. (c, d) The contour plots within the (100) crystal face of calculated partial charge density at *CBM* and *VBM* states, respectively. The isosurfaces are set to 0.001 eV/Å^3.

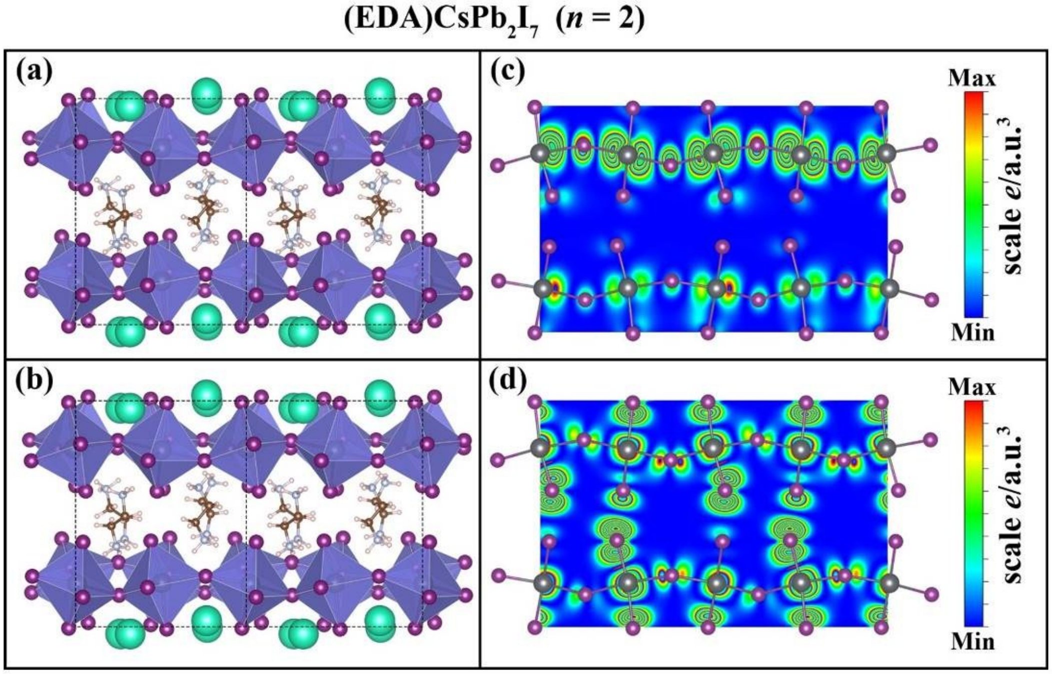

Figure S17. (a, b) The optimized polyhedron model of 1×2×1 supercell of (EDA)$Cs_{n-1}Pb_nI_{3n+1}$ ($n = 2$) from the view of *c* axis. (c, d) The contour plots within the (100) crystal face of calculated partial charge density at *CBM* and *VBM* states, respectively. The isosurfaces are set to 0.001 eV/Å^3.

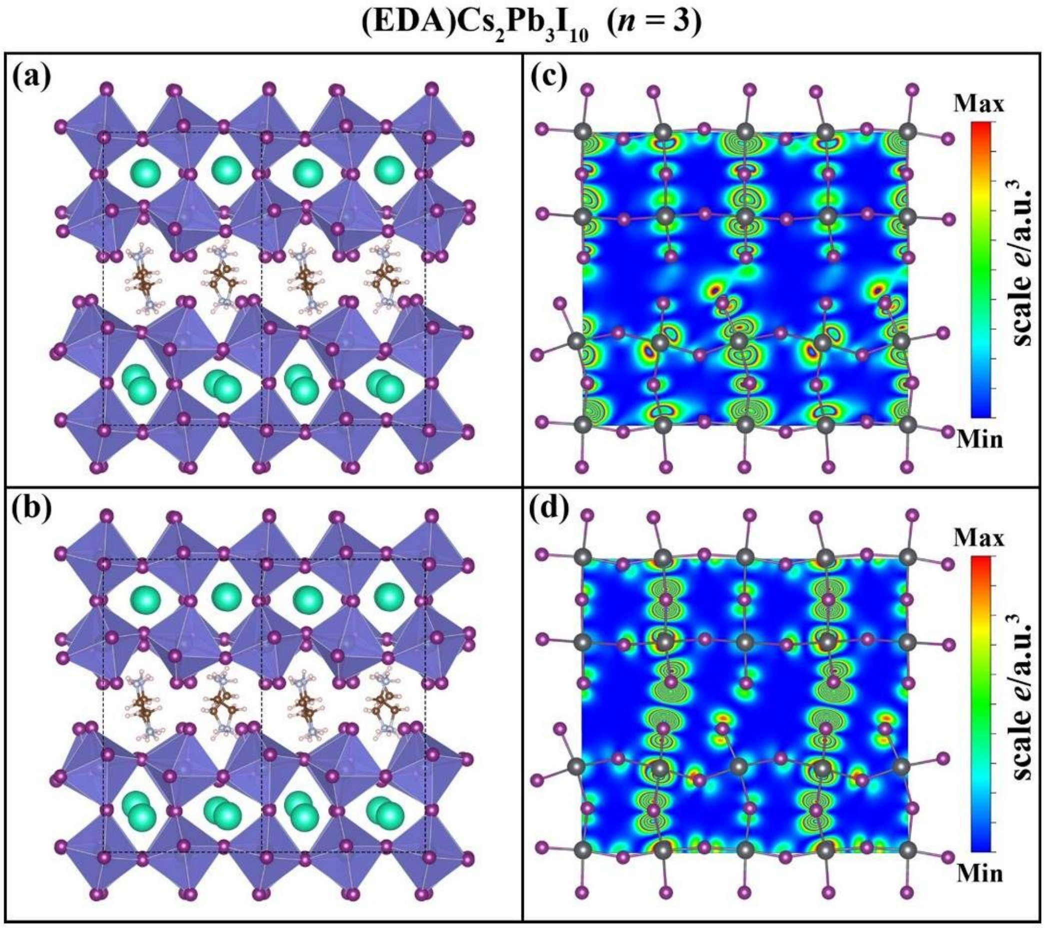

Figure S18. (a, b) The optimized polyhedron models of 1×2×1 supercell of (EDA)$Cs_{n-1}Pb_nI_{3n+1}$ ($n = 3$) from the view of *c* axis. (c, d) The contour plots within the (100) crystal face of calculated partial charge density at *CBM* and *VBM* states, respectively. The isosurfaces are set to 0.001 eV/Å^3.

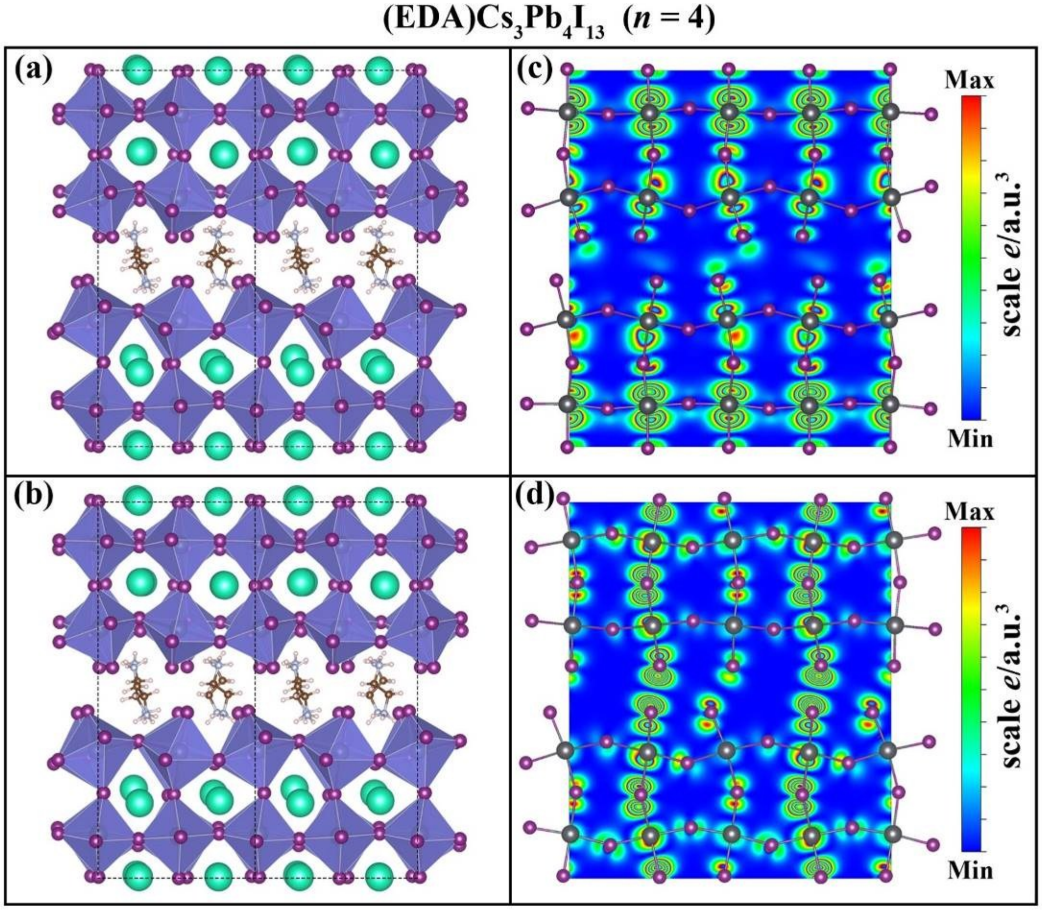
$(EDA)Cs_3Pb_4I_{13}$ ($n = 4$)

Figure S19. (a, b) The optimized polyhedron model of 1×2×1 supercell of $(EDA)Cs_{n-1}Pb_nI_{3n+1}$ ($n = 4$) from the view of *c* axis. (c, d) The contour plots within the (100) crystal face of calculated partial charge density at *CBM* and *VBM* states, respectively. The isosurfaces are set to 0.001 eV/Å^3.

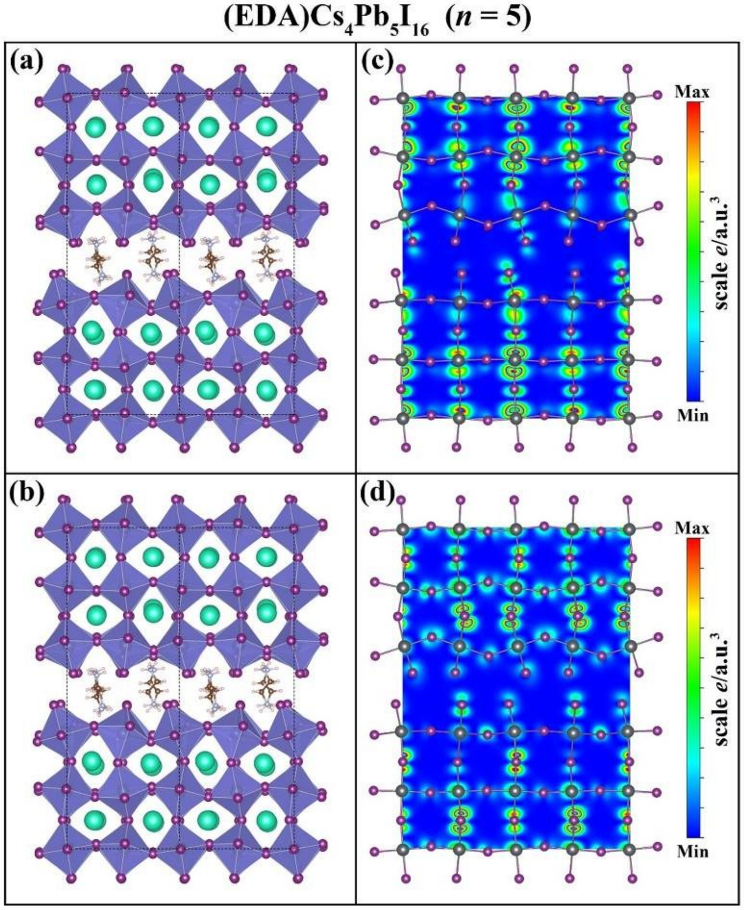
(EDA)$Cs_4Pb_5I_{16}$ (n = 5)

Figure S20. (a, b) The optimized polyhedron model of 1×2×1 supercell of (EDA)$Cs_{n-1}Pb_nI_{3n+1}$ (n = 5) from the view of *c* axis. (c, d) The contour plots within the (100) crystal face of calculated partial charge density at *CBM* and *VBM* states, respectively. The isosurfaces are set to 0.001 eV/Å^3.

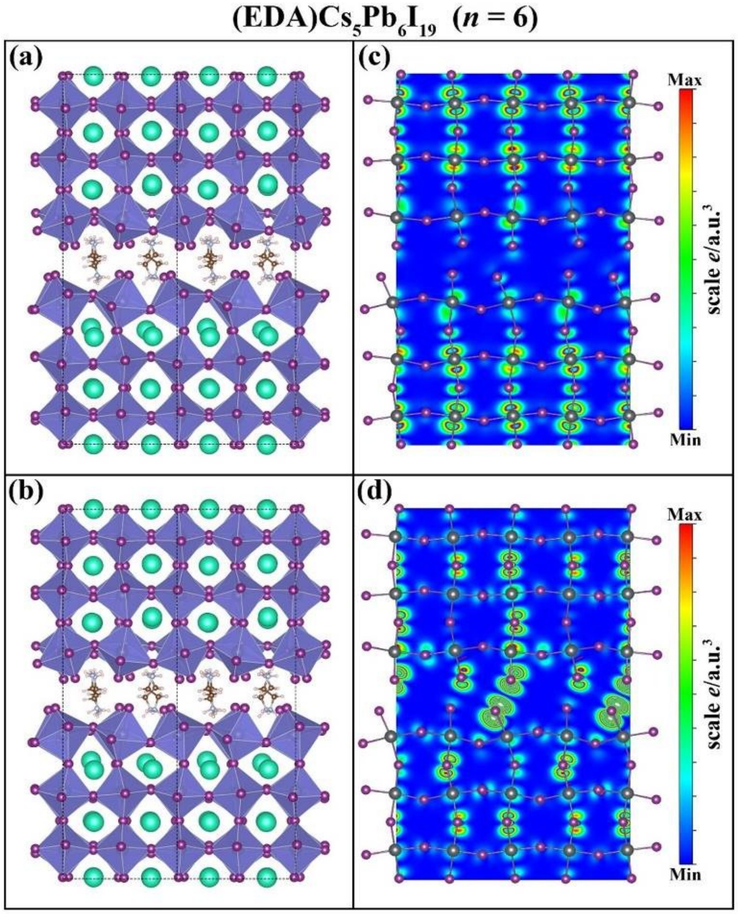

Figure S21. (a, b) The optimized polyhedron model of 1×2×1 supercell of (EDA)Cs$_{n-1}$Pb$_n$I$_{3n+1}$ (n = 6) from the view of c axis. (c, d) The contour plots within the (100) crystal face of calculated partial charge density at *CBM* and *VBM* states, respectively. The isosurfaces are set to 0.001 eV/Å^3.

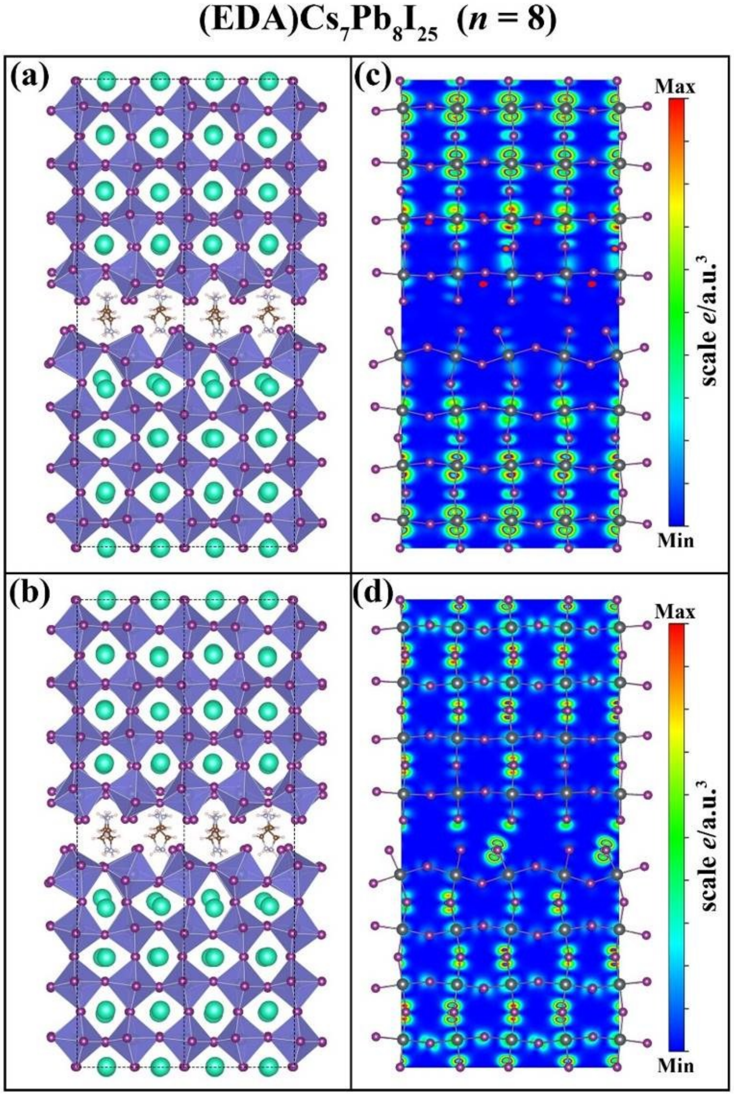

(EDA)$\mathrm{Cs}_7\mathrm{Pb}_8\mathrm{I}_{25}$ (n = 8)

Figure S22. (a, b) The optimized polyhedron model of 1×2×1 supercell of (EDA)$\mathrm{Cs}_{n\text{-}1}\mathrm{Pb}_n\mathrm{I}_{3n+1}$ (n = 8) from the view of *c* axis. (c, d) The contour plots within the (100) crystal face of calculated partial charge density at *CBM* and *VBM* states, respectively. The isosurfaces are set to 0.001 eV/Å^3.

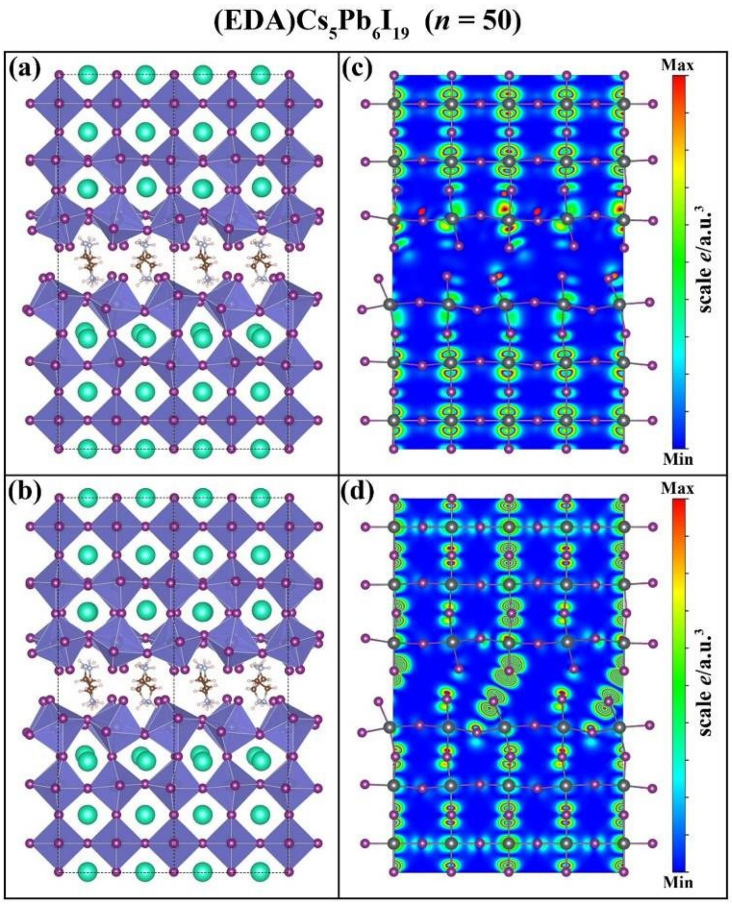

Figure S23. (a, b) The optimized polyhedron model of 1×2×1 supercell of (EDA)$Cs_{n-1}Pb_nI_{3n+1}$ (n = 50) from the view of c axis. (c, d) The contour plots within the (100) crystal face of calculated partial charge density at *CBM* and *VBM* states, respectively. The isosurfaces are set to 0.001 eV/Å^3.

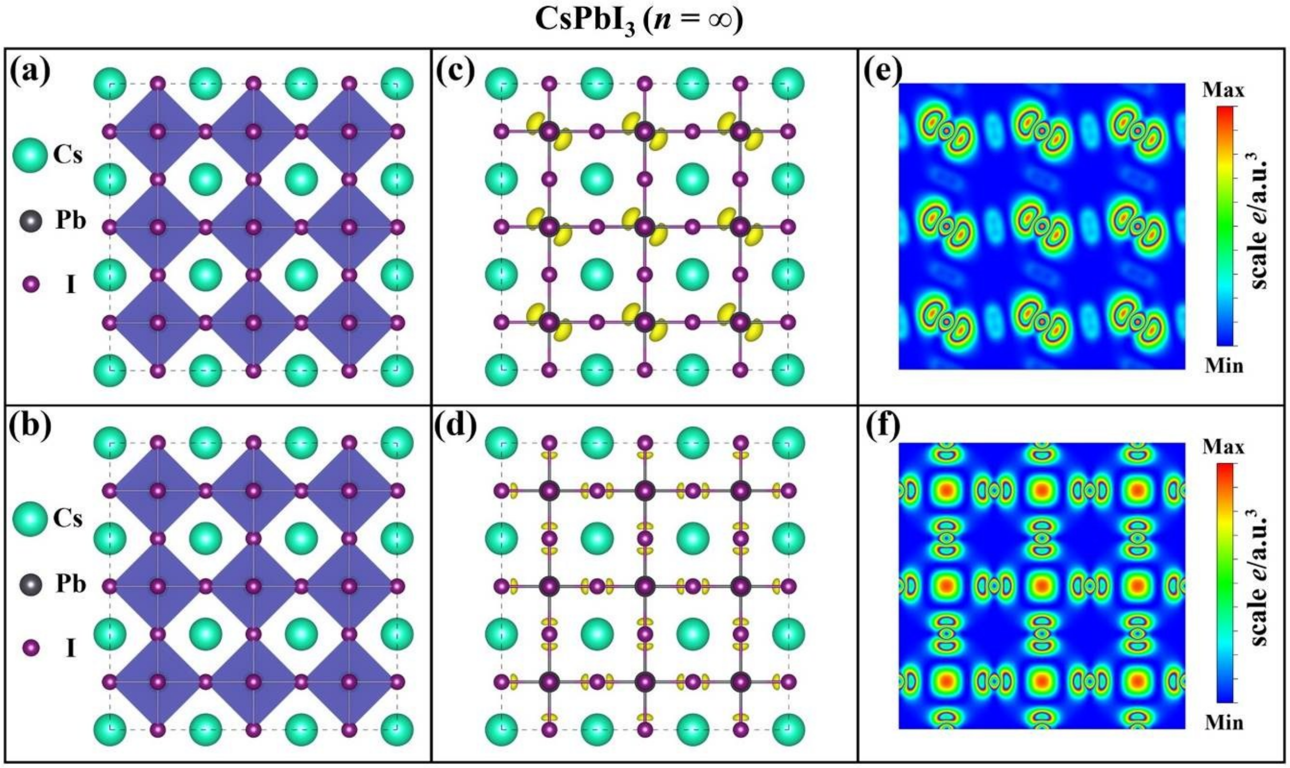

Figure S24. (a, b) The optimized polyhedron model of 3×3×3 supercell of $CsPbI_3$ unit cell from the view of *c* axis. (c, d) Calculated partial charge densities of *CBM* and VBM states, respectively. (e, f) Their contour plots within the (001) crystal face. The isosurfaces are set to 0.001 eV/Å^3.

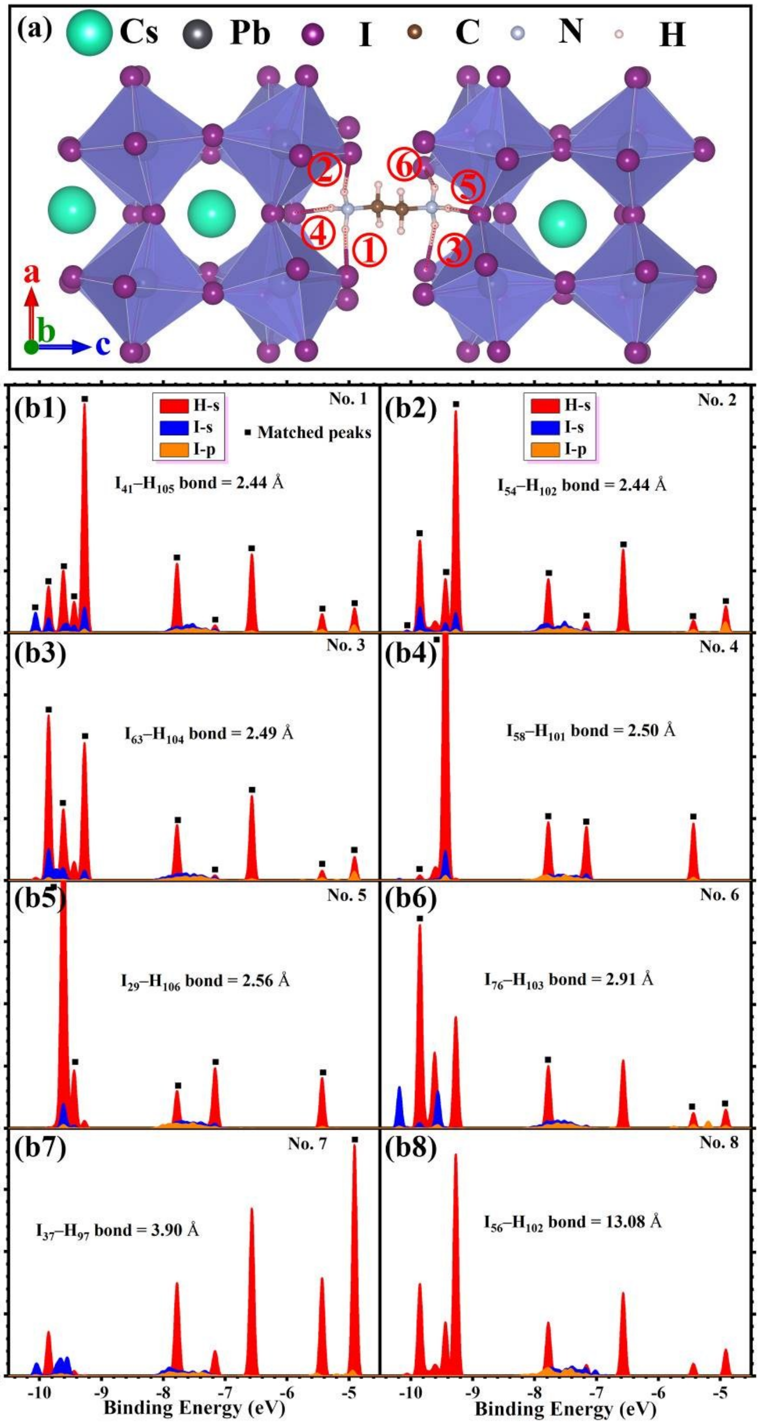

Figure S25. (a) The crystal structure showing six I···H bonds numbered by No. 1-6. (b1-b8) The PDOS for six couples of I and H (of NH_3^+) with I−H bonding (No. 1-6) as well as other two pairs of I and H without chemical interaction (No. 7, 8).

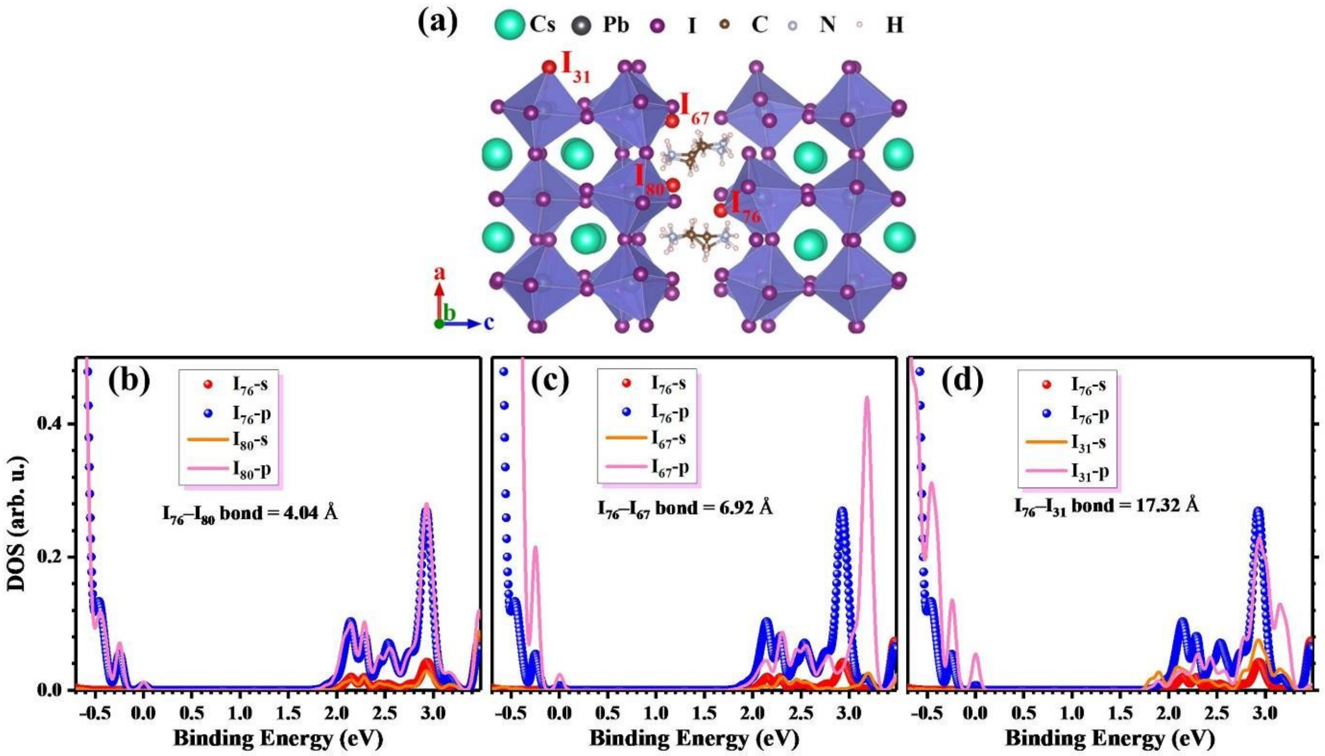

Figure S26. (a) Different I atoms for (EDA)$Cs_{n-1}Pb_nI_{3n+1}$ (n = 4) with labeled by red spheres and numbered by 31, 67, 76 and 80 (I_{67}, I_{76} and I_{80} are terminal I, while I_{31} is inside I). (b-d) PDOS of these I.

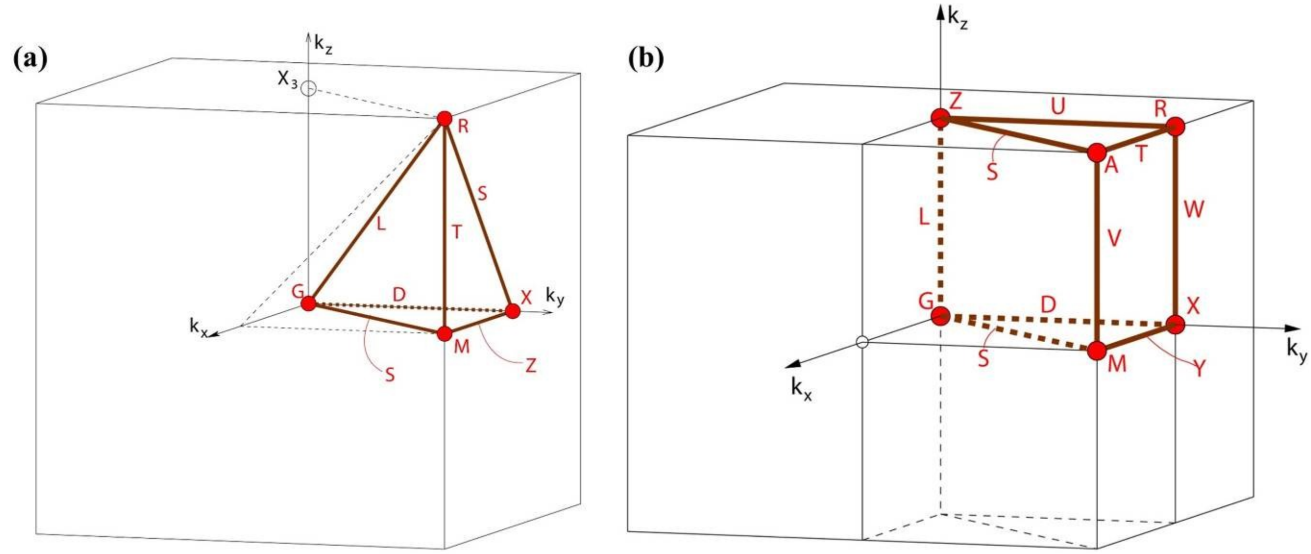

Cubic: *Pm-3m* (221)

Tetragonal: *P4/mbm* (127)

Figure S27. (a, b) The Brillouin zone and *k*-vector types of space group *Pm-3m* (No. 221) and *P4/mbm* (No. 127), respectively. The *k*-point path for band structure of pristine $CsPbI_3$ unit cell and $(EDA)Cs_{n-1}Pb_nI_{3n+1}$ are Γ→X→R→M→Γ and M→Γ→X→R→Z→A, respectively. M(½, ½, 0), Γ(0, 0, 0), X(0, ½, 0), Z(0, 0, ½), A(½, ½, ½), R(½, ½, ½) are for No. 221, and R(0, ½, ½) is for No. 127.[23, 24]

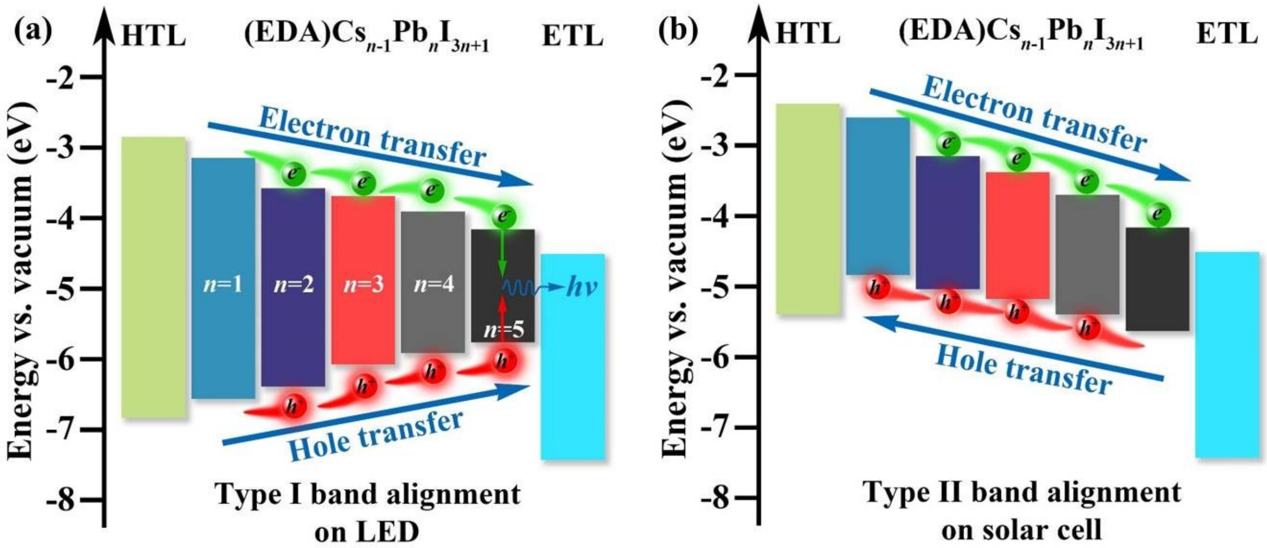

Figure S28. (a) Form left to right, the *CBM* and *VBM* approximate locations of *HTL*, quasi-2D PVSKs, 3D PVSK and *ETL* in a LED based on quasi-2D PVSKs make the type-I band alignment. (b) From left to right, the *CBM* and *VBM* energies of *HTL*, quasi-2D PVSKs, 3D PVSK and *ETL* in a solar cell make the type-II band alignment.

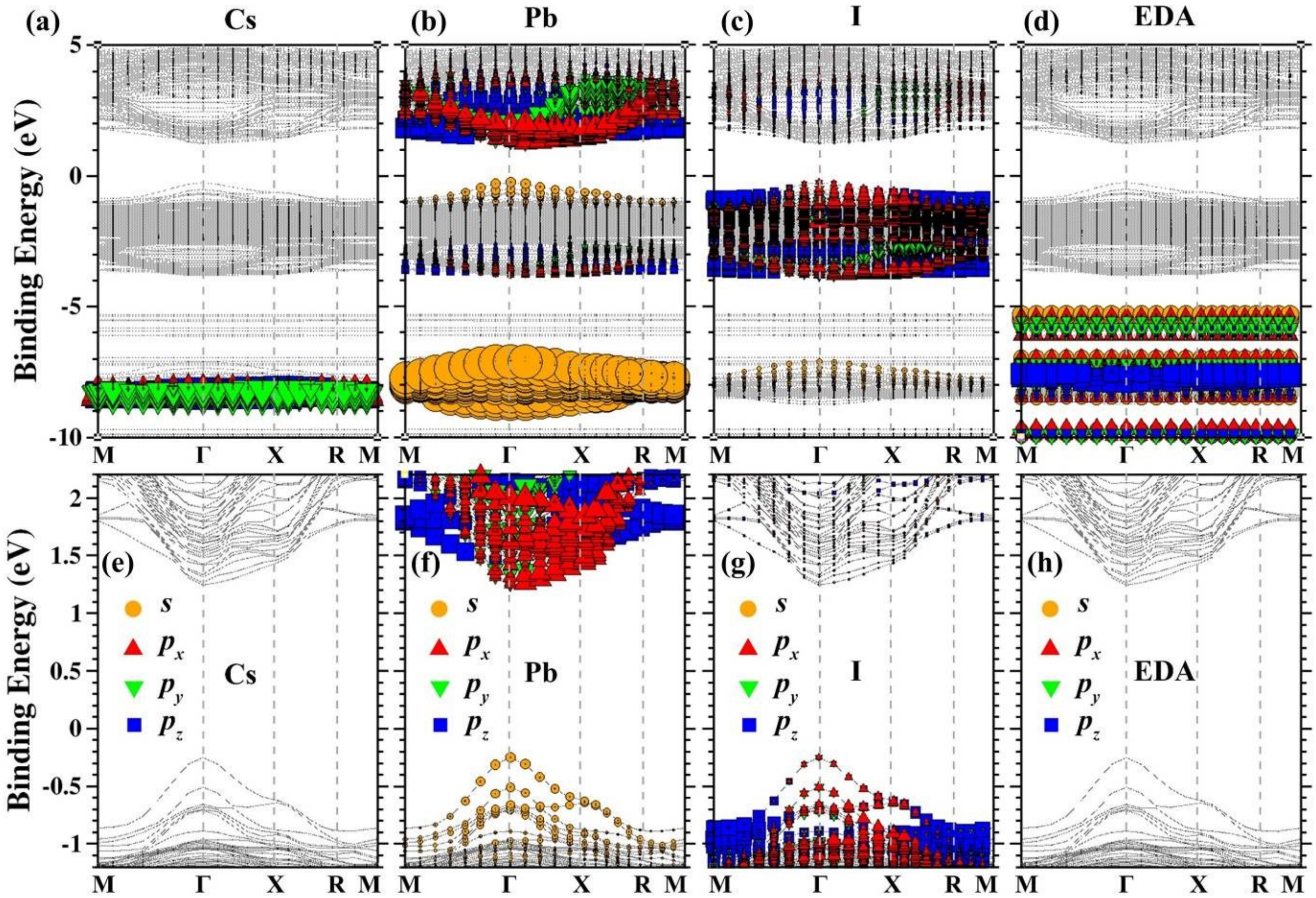

Figure S29. The electronic band structure of (EDA)$Cs_{n-1}Pb_nI_{3n+1}$ PVSKs and the orbital distributions of (a, e) Cs^+, (b, f) Pb^{2+}, (c, g) I^- and (d, h) EDA^{2+} ions as well as their partial enlarged patterns around *VBM* and *CBM*. The sizes of symbols represent the contents of the orbitals.

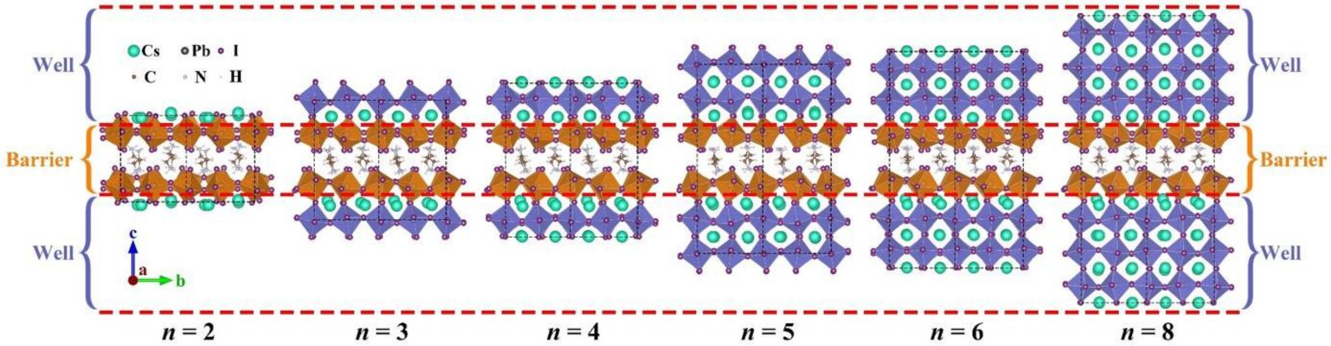

Figure S30. The schemes of barrier and well layer to show the formation of quantum-well (QW) structures in $(EDA)Cs_{n\text{-}1}Pb_nI_{3n+1}$ PVSKs.

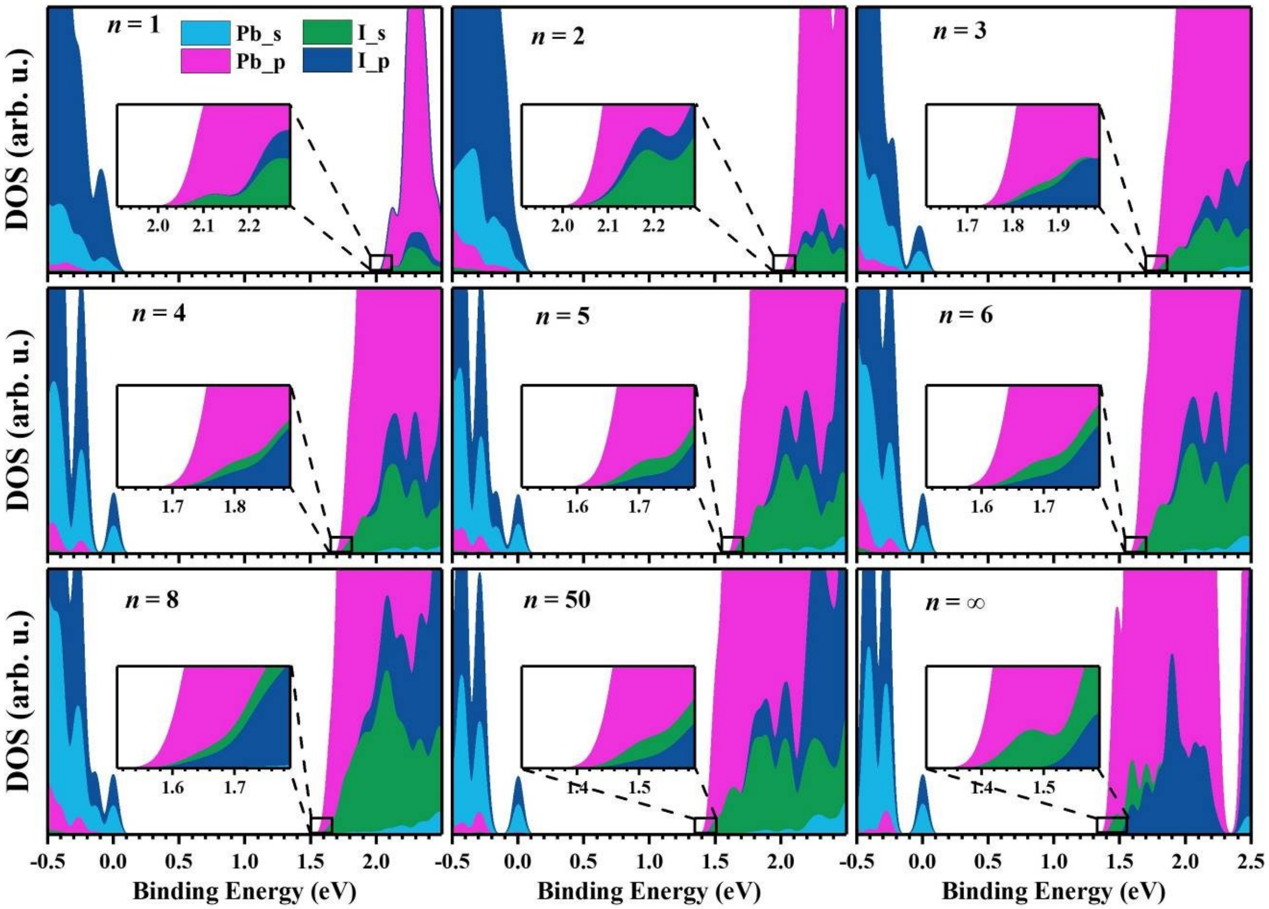

Figure S31. The calculated density of states (DOS) of different orbitals of (EDA)$Cs_{n-1}Pb_nI_{3n+1}$ (n = 1-6, 8, 50 and ∞). The insets are the corresponding enlargements around *CBM*.

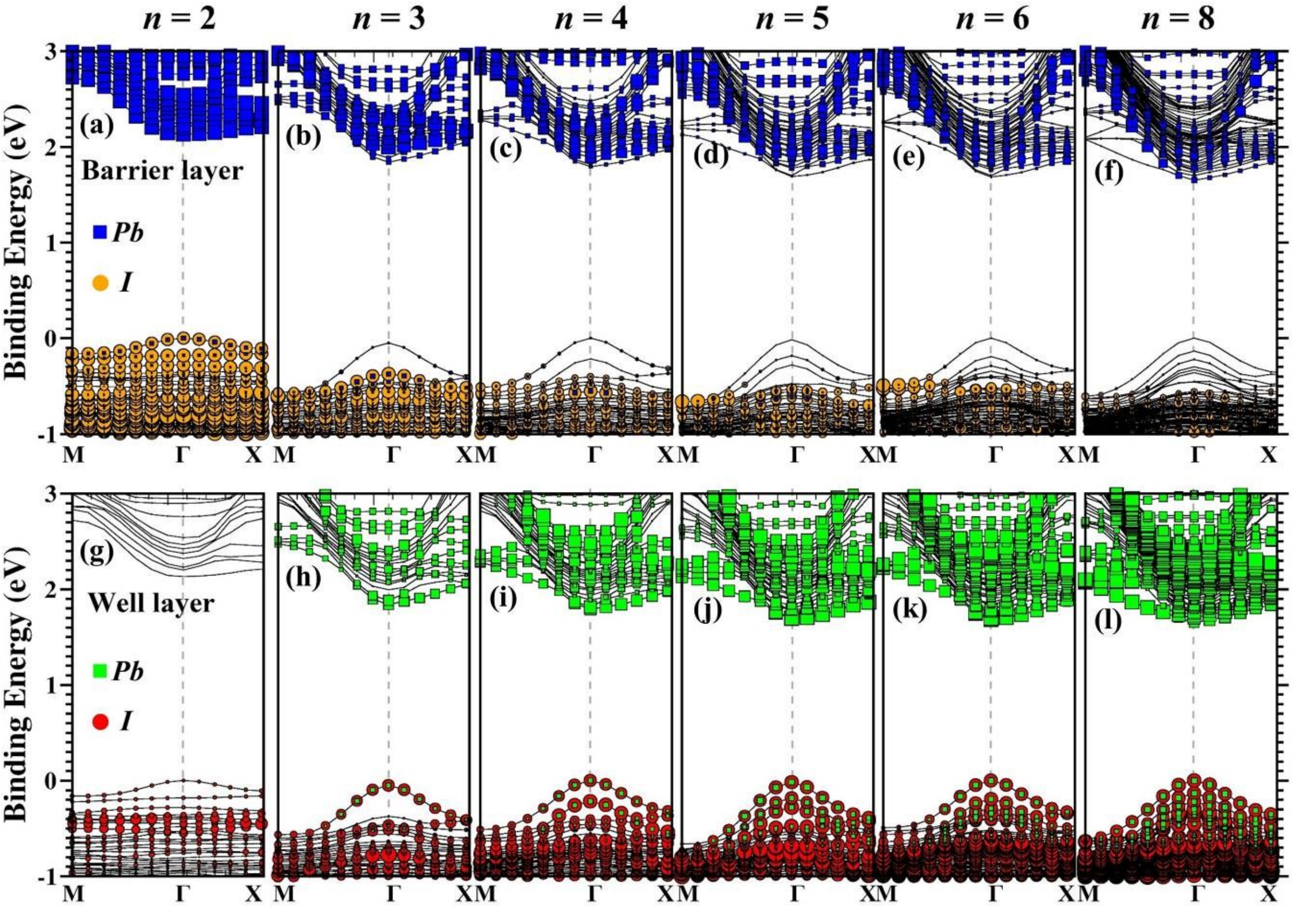

Figure S32. The fatband structures of barrier and well layers for (EDA)$Cs_{n-1}Pb_nI_{3n+1}$ PVSKs as quantum-well (QW) structures.

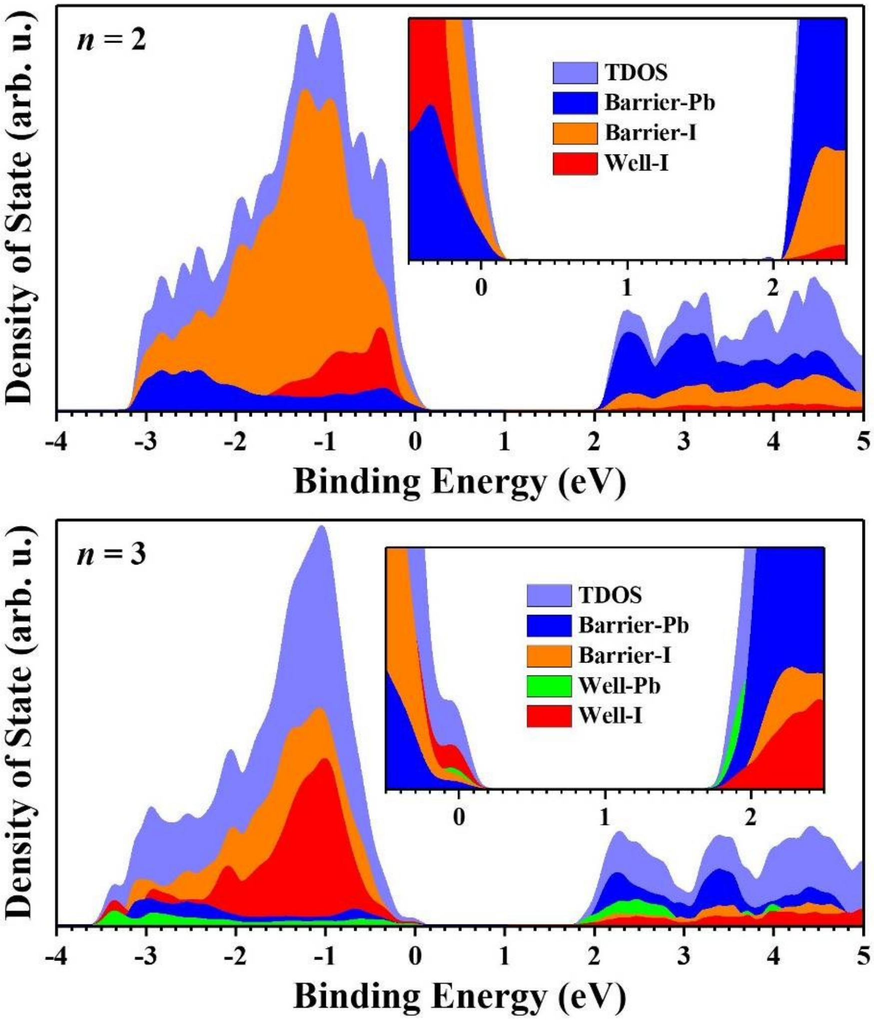

Figure S33. The DOS of barrier and well layers for (EDA)$Cs_{n-1}Pb_nI_{3n+1}$ PVSKs (n = 2, 3) as QW structures.

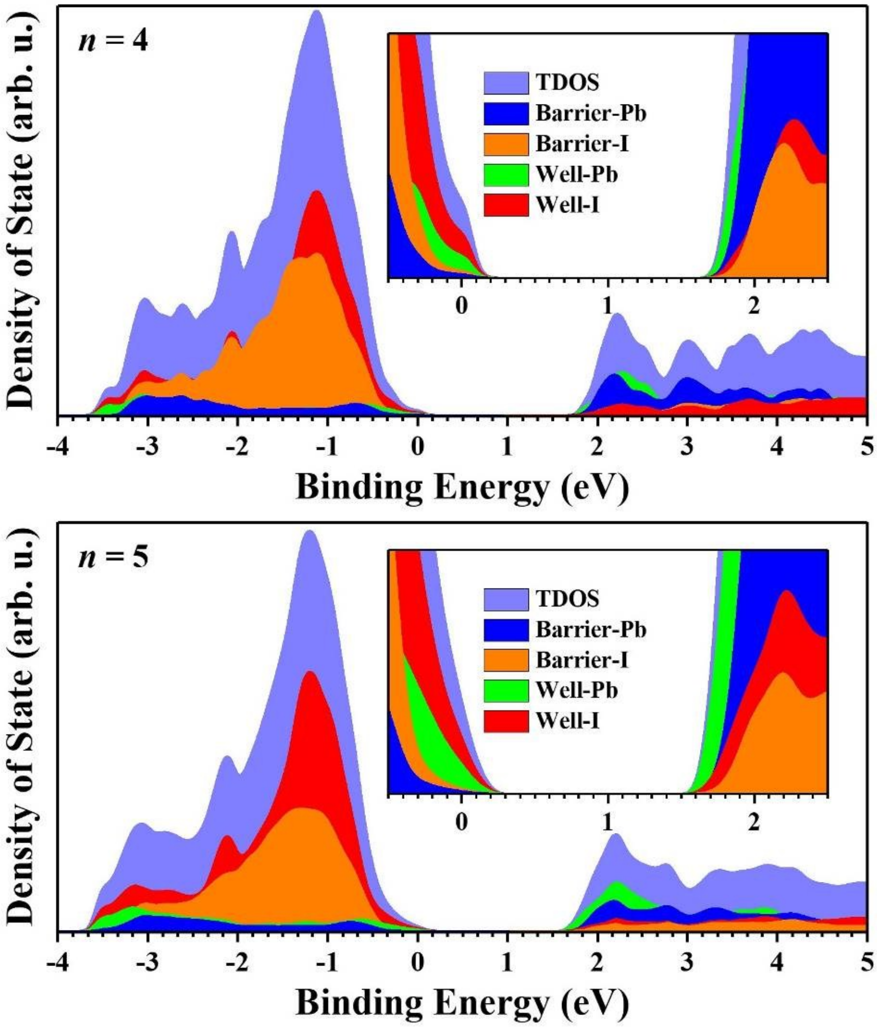

Figure S34. The DOS of barrier and well layers for (EDA)$Cs_{n-1}Pb_nI_{3n+1}$ PVSKs (n = 4, 5) as QW structures.

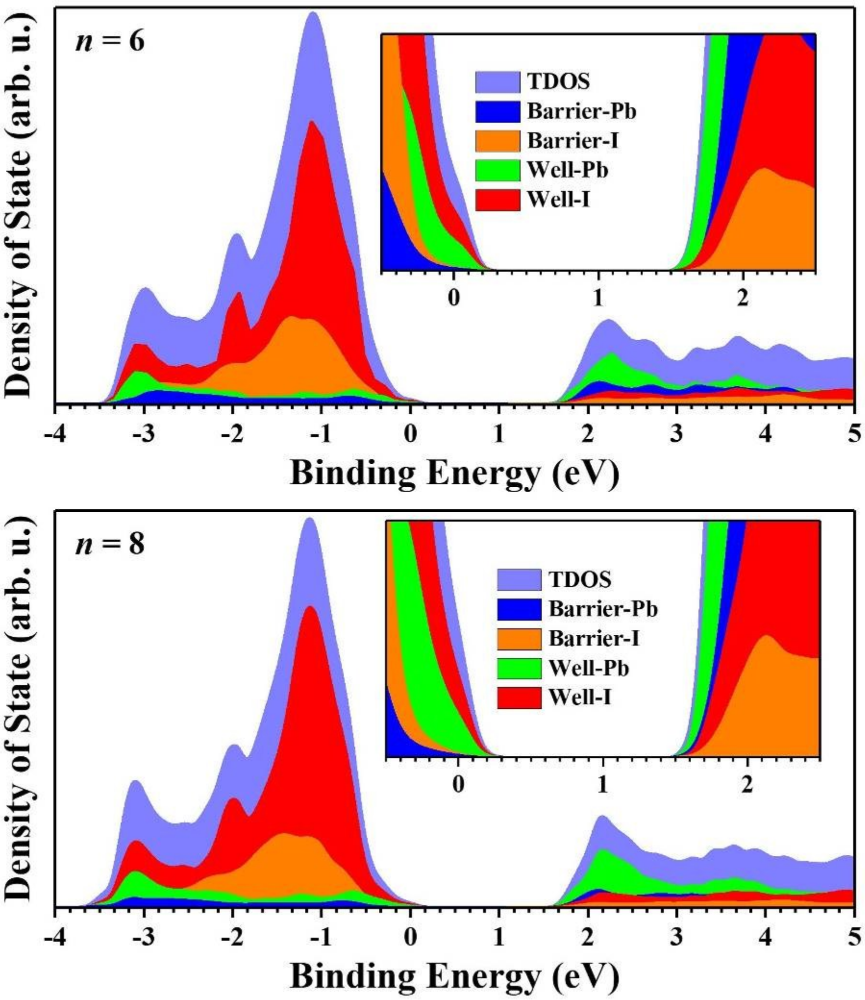

Figure S35. The DOS of barrier and well layers for (EDA)$Cs_{n-1}Pb_nI_{3n+1}$ PVSKs (n = 6, 8) as QW structures.

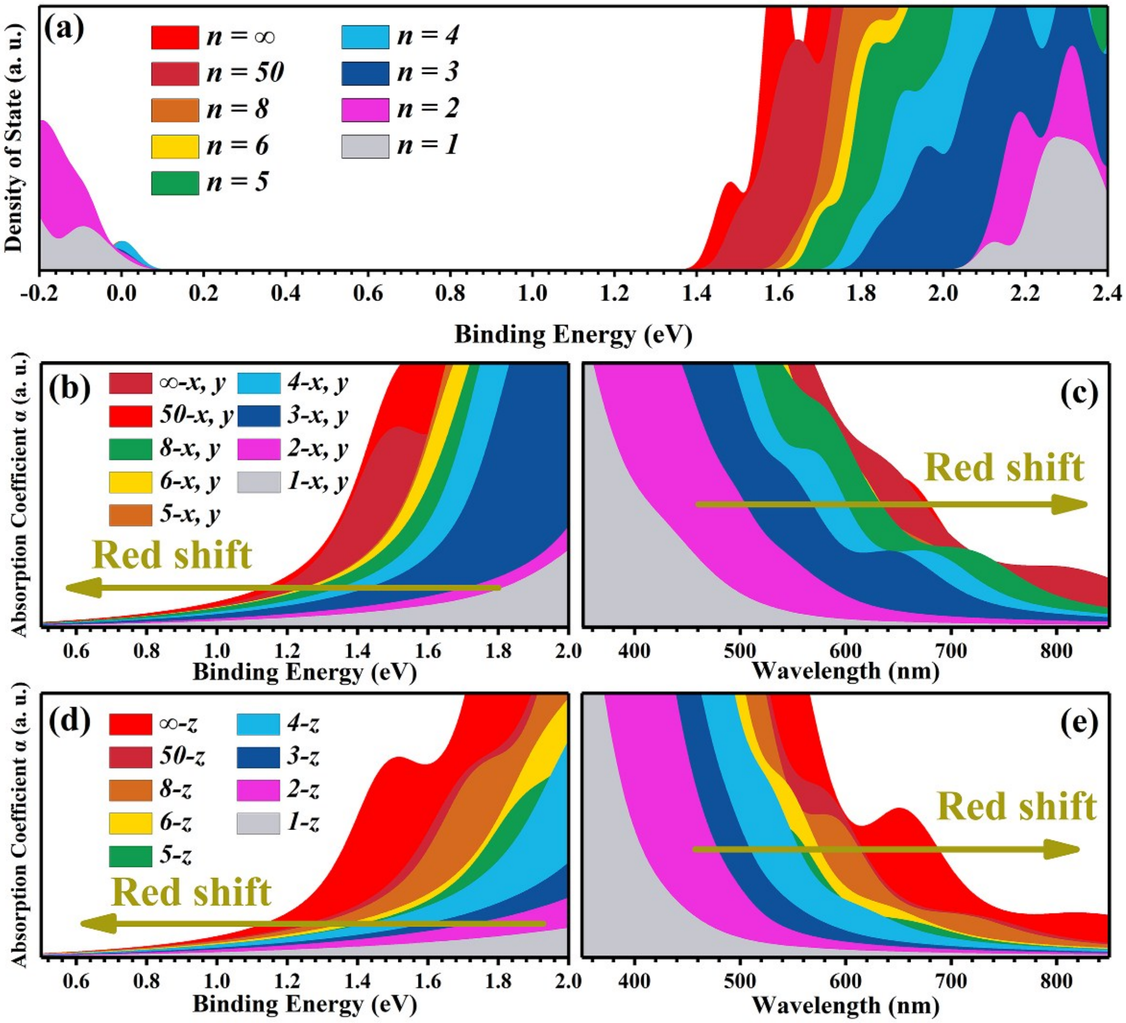

Figure S36. (a) DOS. (b-e) The calculated photo-adsorption spectra of (EDA)$Cs_{n-1}Pb_{n}I_{3n+1}$ PVSKs with different n values *vs.* binding energies and *vs.* wavelengths along x, y and z axis.

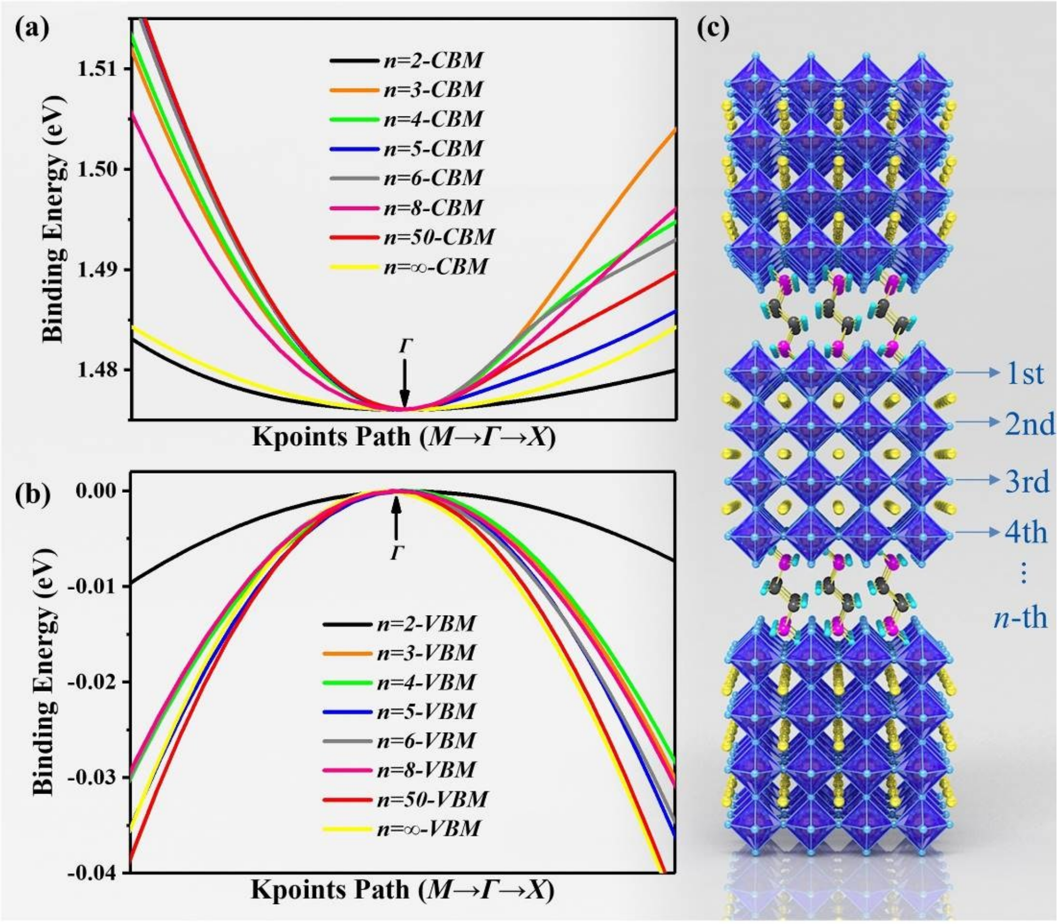

Figure S37. The bands of *VBM* and *CBM* of (EDA)$Cs_{n-1}Pb_nI_{3n+1}$ with n = 2-6, 8, 50 and ∞ from the *k*-points path $M \rightarrow \Gamma \rightarrow X$. A more bent parabolic band means a smaller carriers effective mass.

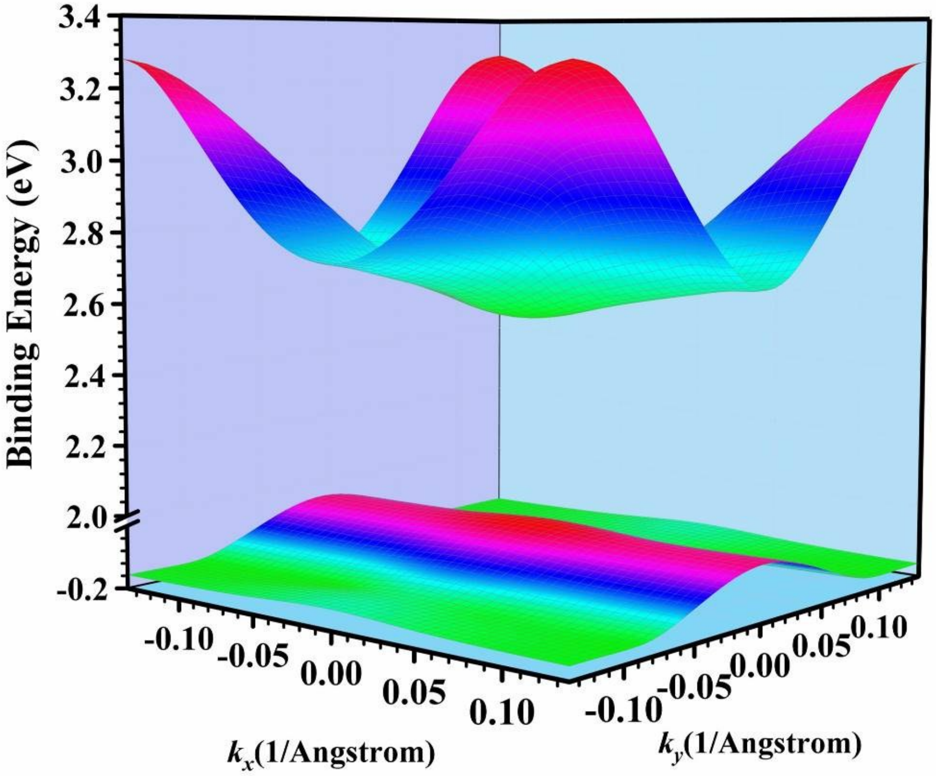

Figure S38. 3D band of *LUMO* and *HOMO* in entire brillouin area for (EDA)$Cs_{n-1}Pb_nI_{3n+1}$ (n = 1) with 2500 *k*-points separation.

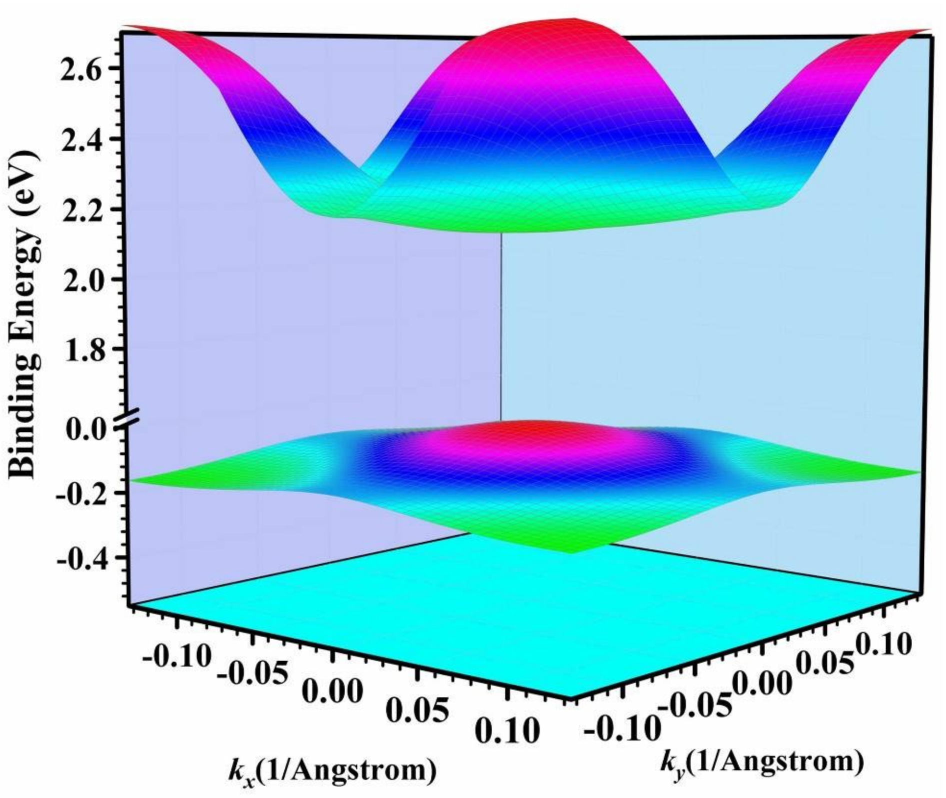

Figure S39. 3D-band of *LUMO* and *HOMO* in entire brillouin area for (EDA)$Cs_{n-1}Pb_nI_{3n+1}$ (n = 2) with 2500 *k*-points separation.

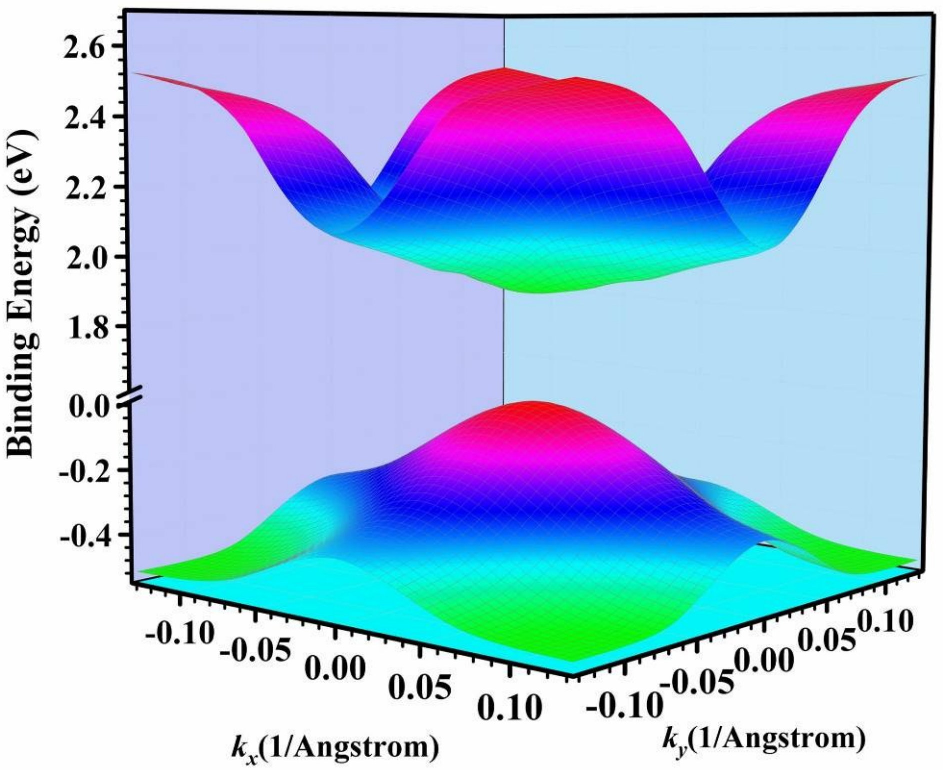

Figure S40. 3D-band of *LUMO* and *HOMO* in entire brillouin area for (EDA)$Cs_{n-1}Pb_nI_{3n+1}$ (n = 3) with 2500 *k*-points separation.

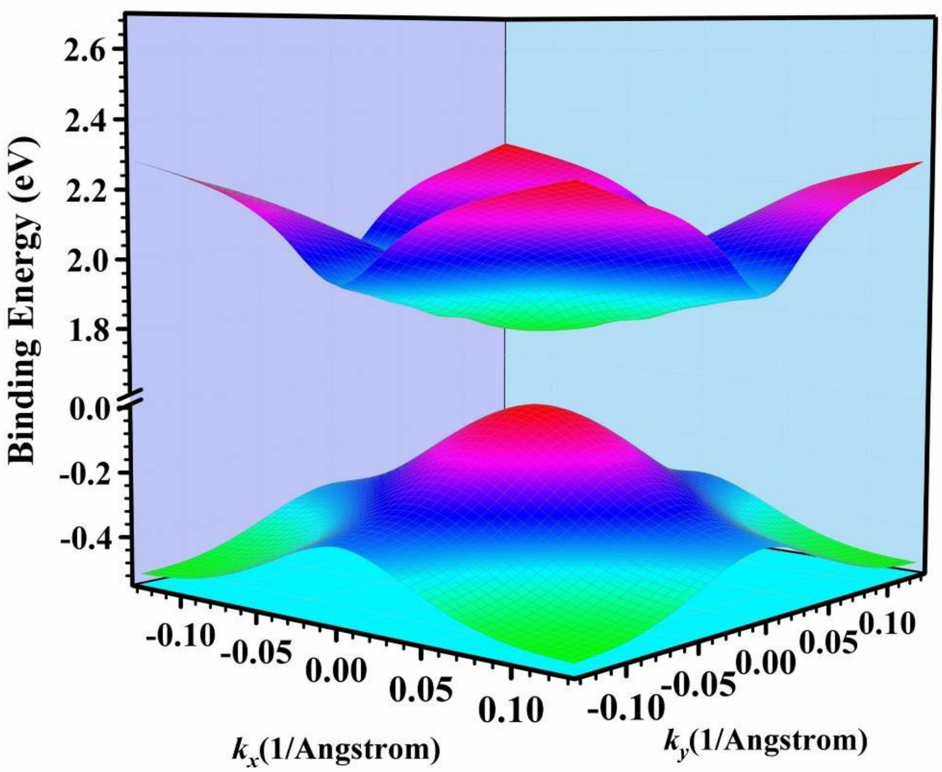

Figure S41. 3D-band of *LUMO* and *HOMO* in entire brillouin area for (EDA)$Cs_{n-1}Pb_nI_{3n+1}$ ($n = 4$) with 2500 *k*-points separation.

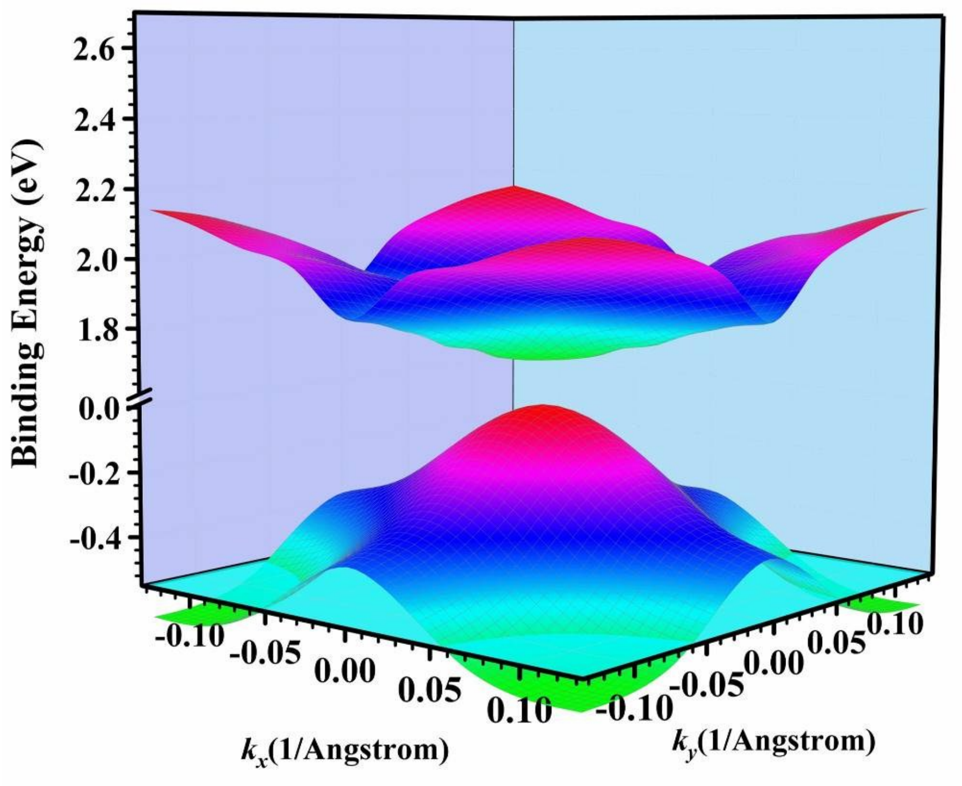

Figure S42. 3D-band of *LUMO* and *HOMO* in entire brillouin area for (EDA)$Cs_{n-1}Pb_nI_{3n+1}$ (n = 5) with 2500 *k*-points separation.

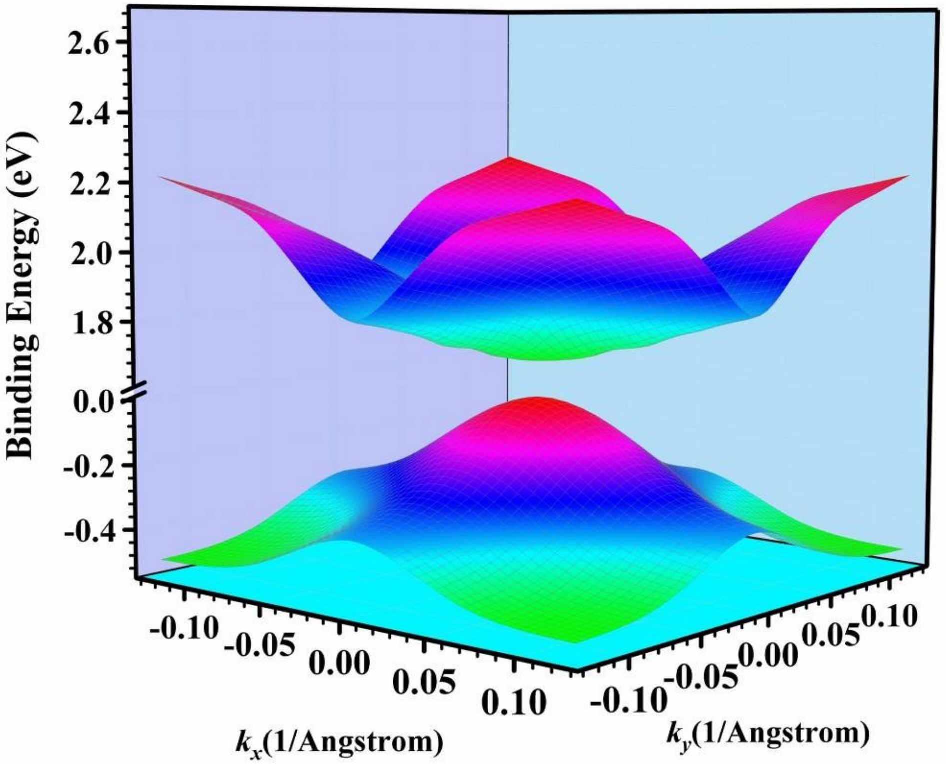

Figure S43. 3D-band of *LUMO* and *HOMO* in entire brillouin area for (EDA)$Cs_{n-1}Pb_nI_{3n+1}$ (n = 6) with 2500 *k*-points separation.

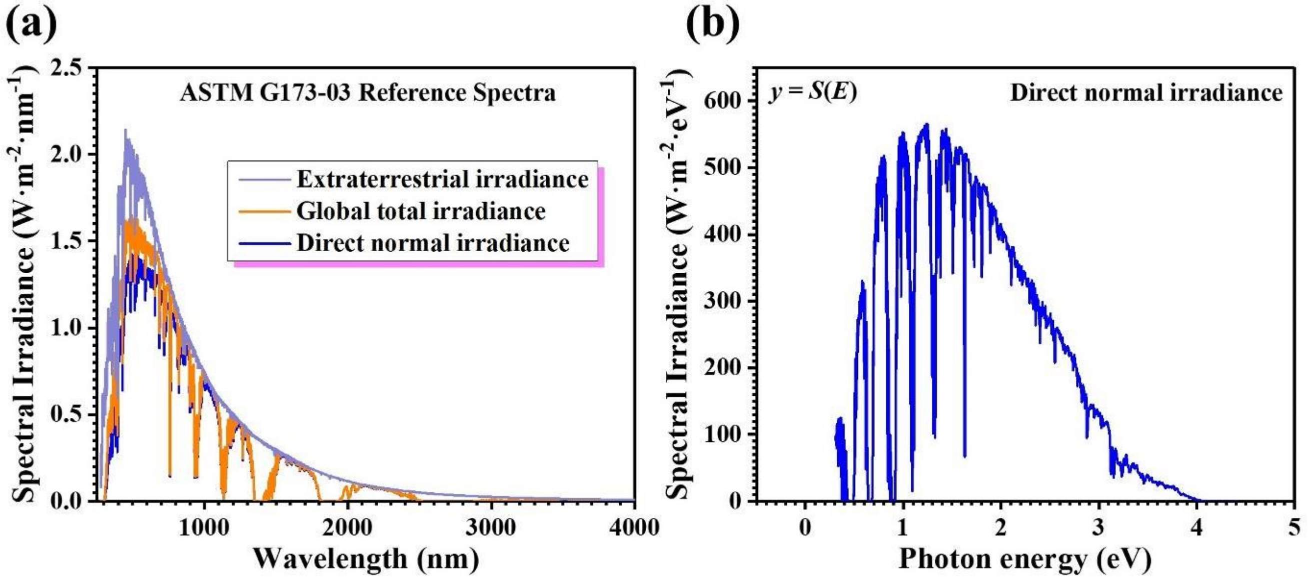

Figure S44. (a) The reference AM 1.5 spectral with different measurement standard reported on the National Renewable Energy Laboratory (NREL) Web site. (b) The direct normal spectral irradiance vs. photon energy, which is defined as the function $S(E)$.

Crystallographic details of quasi-2D DJ α-$CsPbI_3$ PVSKs

Table S1. Calculated lattice parameters of (EDA)$Cs_{n-1}Pb_nI_{3n+1}$ perovskites.

n =	***1***	***2***	***3***	***4***	***5***
a(Å)	12.1638(0)	12.2676(3)	12.3358(7)	12.3748(2)	12.4144(1)
b(Å)	12.1609(8)	12.2662(3)	12.3349(5)	12.3740(4)	12.4140(6)
c(Å)	9.4936(7)	15.8642(2)	22.1881(6)	28.5662(1)	34.9911(9)
α	90.0277(8)	90.0222(7)	90.0198(7)	90.0149(9)	90.0170(7)
β	89.9574(7)	89.9642(6)	89.9694(2)	89.9745(6)	89.9795(3)
γ	91.2001(3)	91.0036(2)	90.8341(1)	90.7134(3)	90.6243(0)
Number of atom	76	96	116	136	156
V(Å³)	1404.0306(9)	2386.8429(6)	3375.8449(4)	4373.9064(1)	5392.2840(3)
n =	***6***	***8***	***45***	**∞ (2×2×2)**	**∞(unit cell)**
a(Å)	12.5879(9)	12.4700(3)	12.5945(7)	12.7798(4)	6.3899(2)
b(Å)	12.5989(7)	12.6498(4)	12.5947(9)	12.7798(4)	6.3899(2)
c(Å)	40.8236(5)	53.8106(1)	40.9483(9)	12.7798(4)	6.3899(2)
α	90.0037(2)	90.0068(9)	89.9309(9)	90.0000(0)	90.0000(0)
β	89.9887(6)	89.9904(5)	90.0217(5)	90.0000(0)	90.0000(0)
γ	90.3056(0)	90.0966(0)	90.2973(8)	90.0000(3)	90.0000(3)
Number of atom	176	216	176	40	5
V(Å³)	6474.3626(5)	8347.4002(8)	6495.3851(7)	2087.2604(8)	260.9075(6)

Table S2. Pb-I bond lengths and I-Pb-I angles of (EDA)PbI$_4$ (n = 1) perovskites.

Label	*i-th layer*	*1*
Pb-I bond	*Equatorial*	3.2355(4)
	Apical	3.1634(2)
	Average	3.1994(8)
I-Pb-I angle	*Equatorial*	174.8979(6)
	Apical	173.3063(5)
	Average	174.1021(6)
Pb-I-Pb angle	*Equatorial*	126.6005(7)
	Apical	-
	Average	126.6005(7)

Table S3. Pb-I bond lengths and I-Pb-I angles of (EDA)CsPb$_2$I$_7$ (n = 2) perovskites.

Label	*i-th layer*	*1*	*2*
Pb-I bond	*Equatorial*	3.2786(0)	3.2287(1)
	Apical	3.1934(2)	3.2265(1)
	Average	3.2360(1)	3.2276(1)
I-Pb-I angle	*Equatorial*	169.5892(3)	170.3656(4)
	Apical	171.3682(8)	162.1338(8)
	Average	170.4787(5)	166.2497(6)
Pb-I-Pb angle	*Equatorial*	131.0102(1)	129.7096(3)
	Apical	128.9670(3)	-
	Average	129.9886(2)	129.7096(3)

Table S4. Pb-I bond lengths and I-Pb-I angles of (EDA)$Cs_2Pb_3I_{10}$ (n = 3) perovskites.

Label	*i-th layer*	*1*	*2*	*3*
Pb-I bond	*Equatorial*	3.2306(9)	3.1269(5)	3.2366(7)
	Apical	3.2022(3)	3.2252(2)	3.1999(3)
	Average	3.2164(6)	3.1760(8)	3.2183(0)
I-Pb-I angle	*Equatorial*	172.5995(6)	175.5315(9)	175.74381
	Apical	175.3023(3)	175.5195(8)	171.6574(8)
	Average	172.5995(6)	175.5315(9)	175.7438(1)
Pb-I-Pb angle	*Equatorial*	133.2437(0)	146.5855(1)	133.9487(3)
	Apical	138.6423(2)	153.2566(5)	-
	Average	135.9430(1)	149.9210(8)	133.9487(3)

Table S5. Pb-I bond lengths and I-Pb-I angles of (EDA)$Cs_3Pb_4I_{13}$ (n = 4) perovskites.

Label	*i-th layer*	*1*	*2*	*3*	*4*
Pb-I bond	*Equatorial*	3.2483(2)	3.1291(5)	3.1761(7)	3.2473(3)
	Apical	3.2045(6)	3.2191(6)	3.2159(9)	3.1988(4)
	Average	3.2264(4)	3.1741(5)	3.1960(8)	3.2230(8)
I-Pb-I angle	*Equatorial*	172.9829(1)	175.7938(0)	176.8736(5)	175.9444(4)
	Apical	173.9171(5)	173.0285(8)	172.8354(8)	171.5462(5)
	Average	173.4500(3)	174.4111(9)	174.8545(6)	173.7453(4)
Pb-I-Pb angle	*Equatorial*	145.0178(9)	154.0459(3)	164.3676(0)	145.2886(8)
	Apical	161.8866(5)	166.1241(8)	156.0424(8)	-
	Average	153.4522(7)	160.0850(5)	160.2050(4)	145.2886(8)

Table S6. Pb-I bond lengths and I-Pb-I angles of (EDA)$Cs_4Pb_5I_{16}$ ($n = 5$) perovskites.

Label	***i-th layer***	***1***	***2***	***3***	***4***	***5***
Pb-I bond	*Equatorial*	3.2527(7)	3.1372(2)	3.1337(4)	3.1435(4)	3.2192(8)
	Apical	3.2211(5)	3.2269(9)	3.2127(5)	3.2218(6)	3.2166(0)
	Average	3.2369(6)	3.1821(0)	3.1732(5)	3.1827(0)	3.2179(4)
I-Pb-I angle	*Equatorial*	171.3718(1)	175.7663(4)	177.7166(1)	176.6627(3)	174.6627(3)
	Apical	172.4111(5)	176.4677(0)	176.4677(0)	176.0918(0)	174.3212(0)
	Average	171.9832(8)	176.5887(4)	177.0921(6)	176.2054(4)	174.4919(6)
Pb-I-Pb angle	*Equatorial*	149.6468(9)	162.4161(4)	166.2177(3)	165.3789(1)	146.2887(3)
	Apical	157.1323(3)	161.7988(0)	161.4210(8)	158.8691(0)	-
	Average	153.3896(1)	162.1074(7)	163.8194(0)	162.1240(1)	146.2887(3)

Table S7. Pb-I bond lengths and I-Pb-I angles of (EDA)$Cs_5Pb_6I_{19}$ (*n* = 6) perovskites.

Label	***i-th layer***	***1***	***2***	***3***	***4***	***5***	***6***
Pb-I bond	*Equatorial*	3.2940(0)	3.2028(6)	3.1724(0)	3.1773(3)	3.1970(3)	3.2857(8)
	Apical	3.1982(7)	3.2063(5)	3.1740(1)	3.1899(5)	3.2043(5)	3.2016(5)
	Average	3.2461(3)	3.2046(0)	3.1732(0)	3.1836(4)	3.2006(9)	3.2437(2)
I-Pb-I angle	*Equatorial*	171.7010(4)	175.3856(9)	178.3583(6)	177.8917(6)	176.4740(6)	171.6945(4)
	Apical	172.1051(3)	174.3127(5)	175.7659(0)	177.16145	176.8725(3)	170.1711(3)
	Average	171.9030(8)	174.8492(2)	177.0621(3)	177.5266(1)	176.6732(9)	170.9328(3)
Pb-I-Pb angle	*Equatorial*	148.3646(3)	160.4929(3)	164.9344(9)	166.7495(9)	159.2118(5)	146.9129(8)
	Apical	156.8187(0)	158.5236(0)	159.4571(0)	163.2356(0)	155.8850(8)	-
	Average	152.5916(6)	159.5082(6)	162.1957(9)	164.9925(9)	157.5484(6)	146.9129(8)

Table S8. Pb-I bond lengths and I-Pb-I angles of $(EDA)Cs_7Pb_8I_{25}$ (n = 8) perovskites.

Label	***i-th layer***	***1***	***2***	***3***	***4***	***5***	***6***	***7***	***8***
Pb-I bond	*Equatorial*	3.2586(6)	3.1735(1)	3.1726(9)	3.1844(5)	3.1800(9)	3.1877(1)	3.1501(8)	3.2331(4)
	Apical	3.1979(3)	3.2193(7)	3.2051(1)	3.2016(1)	3.2032(8)	3.2021(1)	3.2086(7)	3.1989(9)
	Average	3.2282(9)	3.1964(4)	3.1889(0)	3.1930(3)	3.1916(9)	3.1949(1)	3.1794(2)	3.2160(6)
I-Pb-I angle	*Equatorial*	173.5347(1)	174.9474(0)	177.4513(6)	178.2283(4)	177.2283(4)	177.9611(5)	177.6132(9)	174.5258(5)
	Apical	174.1572(8)	177.5922(3)	176.9211(3)	178.4376(3)	177.4314(8)	176.5268(0)	174.9939(0)	171.8347(0)
	Average	173.8459(9)	176.2698(1)	177.1862(4)	178.4835(9)	177.3299(1)	177.2439(8)	175.8035(9)	173.1802(8)
Pb-I-Pb angle	*Equatorial*	150.2818(0)	164.3370(0)	155.9876(8)	157.4190(1)	156.5108(5)	158.7285(0)	158.7962(4)	146.7553(8)
	Apical	160.3708(0)	165.7827(5)	169.7953(0)	169.1764(0)	166.4079(3)	159.8597(5)	152.3710(8)	-
	Average	155.3263(0)	165.0598(8)	162.8914(9)	163.2977(1)	161.4593(9)	159.2941(3)	155.5836(6)	146.7553(8)

Table S9. The distances between terminal I^- ions as well as the interlayer distance between two neighbored inorganic layers for EDA^{2+} or propane-1, 3-diammonium cation (PDA^{2+}) intercalated PVSKs with different *n* values.

n	$(EDA)Cs_{n-1}Pb_nI_{3n+1}$		$(PDA)Cs_{n-1}Pb_nI_{3n+1}$		$(3AMP)_2Cs_{n-1}Pb_nI_{3n+1}$[25]
	I-I distance	*Interlayer distance*	*I-I distance*	*Interlayer distance*	*I-I distance*
1	3.8987	3.4473	4.6200	4.6134	4.18
2	3.8423	3.5676	4.3327	4.2924	4.05
3	3.9199	3.4778	4.2491	4.2020	4.02
4	3.9339	3.4580	4.1615	4.1232	4.01
5	3.9837	3.5059			
6	3.9731	3.3784			
8	3.9712	3.4006			
45	3.9379	3.3548			

Table S10. The positions of *VBM* and *CBM* in reciprocal space and the energy of *LUMO* or *HOMO* at Γ and Z.

n	E_g	VBM	CBM	c	Γ−Z distance	orbitals	High k-point		Difference
							Γ	Z	$(\lvert\Delta\rvert)$
1	*2.150*	Z	Z	9.494	0.053	HOMO	0.7591	**1.1288**	0.3697
						LUMO	3.2960	**3.2788**	0.0172
2	*2.109*	Γ	Z	15.864	0.032	HOMO	**1.1644**	0.9655	0.1989
						LUMO	3.2963	**3.2733**	0.0230
3	*1.837*	Z	Z	22.188	0.023	HOMO	1.2393	**1.2901**	0.0508
						LUMO	3.1291	**3.1275**	0.0016
4	*1.793*	Γ	Γ	28.566	0.018	HOMO	**1.3001**	1.2738	0.0263
						LUMO	**3.0926**	3.0938	0.0012
5	*1.690*	Z	Z	34.991	0.014	HOMO	1.3292	**1.3465**	0.0173
						LUMO	3.0370	**3.0363**	0.0007
6	*1.684*	Γ	Γ	40.824	0.012	HOMO	**1.1637**	1.1545	0.0092
						LUMO	**2.8476**	2.8480	0.0004
8	*1.651*	Γ	Z	53.811	0.009	HOMO	**1.3048**	1.2993	0.0055
						LUMO	2.9560	**2.9558**	0.0002
50	*1.497*	Γ	Γ	40.948	0.012	LUMO	**1.3322**	1.3265	0.0057
						LUMO	**2.8289**	2.8292	0.0003

Table S11. The calculated bandgaps, effective masses (in m_0, rest mass of electron) of electrons and holes, dielectric constants and exciton binding energies of (EDA)$Cs_{n-1}Pb_nI_{3n+1}$ PVSKs with different *n* value.

n	E_g	m_e^*	m_h^*	μ	ε_∞^{xx}	ε_∞^{yy}	ε_∞^{zz}	E_b^{xx}(meV)	E_b^{xx} (meV)	E_b^{xx} (meV)
1	*2.150*	0.278	0.634	0.193	4.691	4.717	4.565	119.552	118.238	126.242
2	*2.109*	0.891	0.697	0.391	5.062	5.051	5.126	207.471	208.375	202.322
3	*1.837*	0.158	0.226	0.093	5.415	5.052	5.231	43.180	41.825	46.271
4	*1.793*	0.152	0.205	0.087	5.609	5.551	5.513	37.634	38.426	38.957
5	*1.690*	0.163	0.173	0.084	5.805	5.884	5.352	33.915	33.009	39.898
6	*1.684*	0.133	0.185	0.077	5.697	5.744	5.466	32.442	31.912	35.241
8	*1.651*	0.199	0.201	0.100	5.801	5.835	5.644	40.371	39.902	42.648
45	*1.497*	0.149	0.147	0.074	5.908	5.899	5.670	28.890	28.978	31.366
∞	*1.476*	0.767	0.150	0.125	5.948	5.948	5.948	48.230	48.230	48.230

Table S12. Calculated open-circuit voltages, short-circuit currents and power conversion efficiencies for (EDA)$Cs_{n-1}Pb_nI_{3n+1}$ (n = 1-6, 8 and 50) and α-$CsPbI_3$ PVSKs.

n	E_g	V_{OC} (V) (V_{loss} = 0.5 eV)	J_{SC} (mA/cm^2)	η (%)
1	*2.150*	1.650	9.547	12.95%
2	*2.109*	1.609	10.245	13.55%
3	*1.837*	1.337	15.938	17.52%
4	*1.793*	1.293	17.055	18.12%
5	*1.690*	1.190	19.699	19.27%
6	*1.684*	1.184	19.896	19.37%
8	*1.651*	1.151	20.905	19.78%
50	*1.497*	0.997	25.546	20.93%
∞	*1.476*	0.976	26.261	21.07%

Reference

1 J. P. Perdew, K. Burke and M. Ernzerhof, *Phys. Rev. Lett.*, 1996, **77**, 3865-3868.

2 G. Kresse and J. Furthmüller, *Phys. Rev. B*, 1996, **54**, 11169-11186.

3 G. Kresse and D. Joubert, *Phys. Rev. B*, 1999, **59**, 1758-1775.

4 S. Grimme, S. Ehrlich and L. Goerigk, *J. Comput. Chem.*, 2011, **32**, 1456-1465.

5 J. Moellmann and S. Grimme, *J. Phys. Chem. C*, 2014, **118**, 7615-7621.

6 L. Bengtsson, *Phys. Rev. B*, 1999, **59**, 12301-12304.

7 Y. G. Wang, Y. Yoon, V. A. Glezakou, J. Li and R. Rousseau, *J. Am. Chem. Soc.*, 2013, **135**, 10673-10683.

8 W. J. Yin, Y. Yan and S. H. Wei, *J. Phys. Chem. Lett.*, 2014, **5**, 3625-3631.

9 R. Ali, G. J. Hou, Z. G. Zhu, Q. B. Yan, Q. R. Zheng and G. Su, *J. Mater. Chem. A*, 2018, **6**, 9220-9227.

10 M. H. Shang, J. Zhang, P. Zhang, Z. Yang, J. Zheng, M. A. Haque, W. Yang, S. H. Wei and T. Wu, *J. Phys. Chem. Lett.*, 2019, **10**, 59-66.

11 Y. Jiang, J. Yuan, Y. Ni, J. Yang, Y. Wang, T. Jiu, M. Yuan and J. Chen, *Joule*, 2018, **2**, 1356-1368.

12 X. G. Zhao, J. H. Yang, Y. Fu, D. Yang, Q. Xu, L. Yu, S. H. Wei and L. Zhang, *J. Am. Chem. Soc.*, 2017, **139**, 2630-2638.

13 L. Zhang and W. Liang, *J. Phys. Chem. Lett.*, 2017, **8**, 1517-1523.

14 G. Tang, Z. Xiao, H. Hosono, T. Kamiya, D. Fang and J. Hong, *J. Phys. Chem. Lett.*, 2018, **9**, 43-48.

15 B. T. Diroll, H. Zhou and R. D. Schaller, *Adv. Funct. Mater.*, 2018, **28**, 1800945.

16 T. Zhou, M. Wang, Z. Zang and L. Fang, *Adv. Energy Mater.*, 2019, 1900664.

17 M. R. Filip, C. Verdi and F. Giustino, *J. Phys. Chem. C*, 2015, **119**, 25209-25219.

18 H. J. Snaith, *Adv. Funct. Mater.*, 2010, **20**, 13-19.

19 Y. Wang, M. I. Dar, L. K. Ono, T. Zhang, M. Kan, Y. Li, L. Zhang, X. Wang, Y. Yang, X. Gao, Y. Qi, M. Gratzel and Y. Zhao, *Science*, 2019, **365**, 591-595.

20 Reference Solar Spectral Irradiance: Air Mass 1.5, http://rredc.nrel.gov/solar/spectra/am1.5 (accessed: November 2019).

21 S. Yu, Y. Yan, M. Abdellah, T. Pullerits, K. Zheng and Z. Liang, *Small*, 2019, **15**, 1905081.

22 Z. Xiao, W. Meng, J. Wang, D. B. Mitzi and Y. Yan, *Mater. Horiz.*, 2017, **4**, 206-216.

23 A. P. Cracknell and B. Davies, *General introduction and tables of irreducible representations of space groups*, New York: IFI/Plenum, 1979.

24 M. I. Aroyo, D. Orobengoa, G. de la Flor, E. S. Tasci, J. M. Perez-Mato and H. Wondratschek, *Acta Crystallogr. A Found. Adv.*, 2014, **70**, 126-137.

25 L. Mao, W. Ke, L. Pedesseau, Y. Wu, C. Katan, J. Even, M. R. Wasielewski, C. C. Stoumpos and M. G. Kanatzidis, *J. Am. Chem. Soc.*, 2018, **140**, 3775-3783.